Euclid preparation.

BAO analysis of photometric galaxy clustering in configuration space

Euclid Collaboration: V. Duret[⋆,1], S. Escoffier[1], W. Gillard[1], I. Tutusaus[2], S. Camera[3, 4, 5], N. Tessore[6],
F. J. Castander[7, 8], N. Aghanim[9], A. Amara[10], L. Amendola[11], S. Andreon[12], N. Auricchio[13], C. Baccigalupi[14, 15, 16, 17],
M. Baldi[18, 13, 19], S. Bardelli[13], P. Battaglia[13], A. Biviano[15, 14], D. Bonino[5], E. Branchini[20, 21, 12], M. Brescia[22, 23, 24],
J. Brinchmann[25, 26], A. Caillat[27], G. Cañas-Herrera[28, 29], V. Capobianco[5], C. Carbone[30], V. F. Cardone[31, 32],
J. Carretero[33, 34], S. Casas[35, 36], M. Castellano[31], G. Castignani[13], S. Cavuoti[23, 24], K. C. Chambers[37], A. Cimatti[38],
C. Colodro-Conde[39], G. Congedo[40], C. J. Conselice[41], L. Conversi[42, 43], Y. Copin[44], F. Courbin[45, 46], H. M. Courtois[47],
M. Cropper[48], A. Da Silva[49, 50], H. Degaudenzi[51], S. de la Torre[27], G. De Lucia[15], A. M. Di Giorgio[52], H. Dole[9],
F. Dubath[51], X. Dupac[43], S. Dusini[53], A. Ealet[44], M. Farina[52], R. Farinelli[13], S. Farrens[54], F. Faustini[55, 31], S. Ferriol[44],
F. Finelli[13, 56], S. Fotopoulou[57], N. Fourmanoit[1], M. Frailis[15], E. Franceschi[13], M. Fumana[30], S. Galeotta[15], B. Gillis[40],
C. Giocoli[13, 19], J. Gracia-Carpio[58], A. Grazian[59], F. Grupp[58, 60], S. V. H. Haugan[61], W. Holmes[62], F. Hormuth[63],
A. Hornstrup[64, 65], P. Hudelot[66], K. Jahnke[67], M. Jhabvala[68], B. Joachimi[6], E. Keihänen[69], S. Kermiche[1],
A. Kiessling[62], M. Kilbinger[54], B. Kubik[44], M. Kunz[70], H. Kurki-Suonio[71, 72], O. Lahav[6], A. M. C. Le Brun[73],
S. Ligori[5], P. B. Lilje[61], V. Lindholm[71, 72], I. Lloro[74], G. Mainetti[75], D. Maino[76, 30, 77], E. Maiorano[13], O. Mansutti[15],
S. Marcin[78], O. Marggraf[79], K. Markovic[62], M. Martinelli[31, 32], N. Martinet[27], F. Marulli[80, 13, 19], R. Massey[81],
S. Maurogordato[82], E. Medinaceli[13], S. Mei[83, 84], M. Melchior[78], Y. Mellier[85, 66], M. Meneghetti[13, 19], E. Merlin[31],
G. Meylan[86], A. Mora[87], M. Moresco[80, 13], B. Morin[54], L. Moscardini[80, 13, 19], E. Munari[15, 14], R. Nakajima[79],
C. Neissner[88, 34], R. C. Nichol[10], S.-M. Niemi[28], C. Padilla[88], S. Paltani[51], F. Pasian[15], K. Pedersen[89],
W. J. Percival[90, 91, 92], V. Pettorino[28], S. Pires[54], G. Polenta[55], M. Poncet[93], L. A. Popa[94], L. Pozzetti[13], F. Raison[58],
R. Rebolo[39, 95, 96], J. Rhodes[62], G. Riccio[23], E. Romelli[15], M. Roncarelli[13], R. Saglia[60, 58], Z. Sakr[11, 2, 97], D. Sapone[98],
B. Sartoris[60, 15], J. A. Schewtschenko[40], P. Schneider[79], T. Schrabback[99], A. Secroun[1], E. Sefusatti[15, 14, 16], G. Seidel[67],
S. Serrano[8, 100, 7], P. Simon[79], C. Sirignano[101, 53], G. Sirri[19], A. Spurio Mancini[102], L. Stanco[53], J.-L. Starck[54],
J. Steinwagner[58], P. Tallada-Crespí[33, 34], D. Tavagnacco[15], A. N. Taylor[40], I. Tereno[49, 103], S. Toft[104, 105],
R. Toledo-Moreo[106], F. Torradeflot[34, 33], J. Valiviita[71, 72], T. Vassallo[60, 15], G. Verdoes Kleijn[107],
A. Veropalumbo[12, 21, 20], Y. Wang[108], J. Weller[60, 58], G. Zamorani[13], F. M. Zerbi[12], E. Zucca[13], M. Bolzonella[13],
C. Burigana[109, 56], M. Calabrese[110, 30], D. Di Ferdinando[19], J. A. Escartin Vigo[58], L. Gabarra[111], S. Matthew[40],
N. Mauri[38, 19], A. Pezzotta[58], M. Pöntinen[71], C. Porciani[79], V. Scottez[85, 112], M. Tenti[19], M. Viel[14, 15, 17, 16, 113],
M. Wiesmann[61], Y. Akrami[114, 115], V. Allevato[23], I. T. Andika[116, 117], M. Archidiacono[76, 77], F. Atrio-Barandela[118],
A. Balaguera-Antolinez[39, 96], M. Ballardini[119, 13, 120], D. Bertacca[101, 59, 53], M. Bethermin[121], A. Blanchard[2],
L. Blot[122, 73], H. Böhringer[58, 123, 124], S. Borgani[125, 14, 15, 16, 113], M. L. Brown[41], S. Bruton[126], R. Cabanac[2],
A. Calabro[31], B. Camacho Quevedo[8, 7], A. Cappi[13, 82], F. Caro[31], C. S. Carvalho[103], T. Castro[15, 16, 14, 113], F. Cogato[80, 13],
S. Contarini[58], T. Contini[2], A. R. Cooray[127], S. Davini[21], F. De Paolis[128, 129, 130], G. Desprez[107], A. Díaz-Sánchez[131],
S. Di Domizio[20, 21], J. M. Diego[132], A. G. Ferrari[19], P. G. Ferreira[111], A. Finoguenov[71], K. Ganga[83],
J. García-Bellido[114], T. Gasparetto[15], E. Gaztanaga[7, 8, 36], F. Giacomini[19], F. Gianotti[13], G. Gozaliasl[133, 71],
A. Gregorio[125, 15, 16], M. Guidi[18, 13], C. M. Gutierrez[134], A. Hall[40], S. Hemmati[135], H. Hildebrandt[136], J. Hjorth[89],
J. J. E. Kajava[137, 138], Y. Kang[51], V. Kansal[139, 140], D. Karagiannis[119, 141], C. C. Kirkpatrick[69], S. Kruk[43], M. Lattanzi[120],
M. Lembo[119, 120], G. Leroy[142, 81], J. Lesgourgues[35], T. I. Liaudat[143], S. J. Liu[52], A. Loureiro[144, 145], G. Maggio[15],
M. Magliocchetti[52], F. Mannucci[146], R. Maoli[147, 31], J. Martín-Fleitas[87], C. J. A. P. Martins[148, 25], L. Maurin[9],
R. B. Metcalf[80, 13], M. Miluzio[43, 149], P. Monaco[125, 15, 16, 14], C. Moretti[17, 113, 15, 14, 16], C. Murray[83], S. Nadathur[36],
K. Naidoo[36], A. Navarro-Alsina[79], S. Nesseris[114], K. Paterson[67], A. Pisani[1, 150], D. Potter[151], I. Risso[152], P.-F. Rocci[9],
M. Sahlén[153], E. Sarpa[17, 113, 16], A. Schneider[151], D. Sciotti[31, 32], E. Sellentin[154, 155], M. Sereno[13, 19], A. Silvestri[29],
L. C. Smith[156], K. Tanidis[111], C. Tao[1], G. Testera[21], R. Teyssier[150], S. Tosi[20, 152], A. Troja[101, 53], M. Tucci[51],
C. Valieri[19], A. Venhola[157], D. Vergani[13], F. Vernizzi[158], G. Verza[159], P. Vielzeuf[1], and N. A. Walton[156]

(Affiliations can be found after the references)

March 17, 2025

ABSTRACT

With about 1.5 billion galaxies expected to be observed, the very large number of objects in the *Euclid* photometric survey will allow for precise studies of galaxy clustering from a single survey, over a large range of redshifts $0.2 < z < 2.5$. In this work, we use photometric redshifts (z_{ph}) to extract the baryon acoustic oscillation signal (BAO) from the Flagship galaxy mock catalogue with a tomographic approach to constrain the evolution of the Universe and infer its cosmological parameters. We measure the two-point angular correlation function in 13 redshift bins. A template-fitting approach is applied to the measurement to extract the shift of the BAO peak through the transverse Alcock–Paczynski parameter α. A joint analysis of all redshift bins is performed to constrain α at the effective redshift $z_{eff} = 0.77$ with Markov Chain Monte-Carlo and profile likelihood techniques. We also extract one α_i parameter per redshift bin to quantify its evolution as a function of time. From these 13 α_i, which are directly proportional to the ratio $D_A / r_{s,drag}$, we constrain the reduced Hubble constant h, the baryon density parameter Ω_b, and the cold dark matter density parameter Ω_{cdm}. From the joint analysis, we constrain $\alpha(z_{eff} = 0.77) = 1.0011^{+0.0078}_{-0.0079}$ at the 68% confidence level, which represents a three-fold improvement over current constraints from the Dark Energy Survey (uncertainty of ± 0.023 at $z_{eff} = 0.85$ with the same observable). As expected, the constraining power in the analysis of each redshift bin is lower, with an uncertainty ranging from ± 0.13 to ± 0.024. From these results, we constrain h at 0.45%, Ω_b at 0.91%, and Ω_{cdm} at 7.7%. We quantify the influence of analysis choices like the template, scale cuts, redshift bins, and systematic effects like redshift-space distortions over our constraints both at the level of the extracted α_i parameters and at the level of cosmological inference.

Key words. Cosmology: theory – large-scale structure of the Universe – cosmological parameters

1. Introduction

As a stage-IV survey, *Euclid* (Euclid Collaboration: Mellier et al. 2024) was primarily designed to constrain dark energy with two main probes: weak lensing and spectroscopic galaxy clustering. The former will make use of galaxy shapes observed with the Visible Camera (VIS, Euclid Collaboration: Cropper et al. 2024) and their photometric redshifts obtained with the photometer of the Near-Infrared Spectrometer and Photometer (NISP, Euclid Collaboration: Jahnke et al. 2024) together with ground-based observations. The latter will use the precise measurements of galaxy redshifts obtained with the spectrometer of the NISP. *Euclid* will provide a photometric sample of about 1.5 billion galaxies which can be used not only for weak lensing, but also for many other probes like photometric galaxy clustering. The combination of weak gravitational lensing with photometric galaxy clustering will provide strong cosmological constraints (Euclid Collaboration: Blanchard et al. 2020; Tutusaus et al. 2020), which motivates considering this probe in addition to the standard spectroscopic galaxy clustering.

The clustering of galaxies puts constraints on the expansion history of the Universe. One of its most constraining features is the size of the baryon acoustic oscillations (BAO). The BAO scale is a characteristic scale of the Universe which corresponds to the imprint left in the distribution of galaxies by primordial oscillations of the baryons when they were still coupled to photons. These oscillations were created by the interplay between the radiation pressure force supported by photons and the gravitational pull of dark matter overdensities. When baryons and photons decoupled at the drag epoch, oscillations stopped and froze at a scale known as the BAO scale, fixed in comoving coordinates. It can be observed as a peak in the correlation function of the galaxy density field or a succession of peaks in its power spectrum. While it is fixed in comoving coordinates, the apparent size of the BAO scale increases as the Universe expands so that constraining this scale at different redshifts provides information on the expansion rate of the Universe.

The BAO signal is traditionally constrained in 3D with spectroscopic redshifts but given the current accuracy and precision of photometric redshifts, useful information from the BAO signal can also be extracted using photometric samples. The first observations of the BAO signal in galaxy surveys were performed with the Sloan Digital Sky Survey (Eisenstein et al. 2005) and the 2-degree Field Galaxy Redshift Survey

(Percival et al. 2001; Cole et al. 2005) and recently reached new levels of precision with the 0.52% constraints on BAO obtained by the Dark Energy Spectroscopic Instrument first year of observations (DESI Collaboration: Adame et al. 2024). While spectroscopic redshifts measurements provide a very good accuracy, their measurements are too slow to obtain the redshift of all galaxies detected in the photometric sample. *Euclid* uses slitless spectroscopy, allowing the measurement of multiple spectra in a single exposure which mitigates the speed issue. However, the mission optimisation resulted in *Euclid* being capable of reliably detecting emission lines down to a flux limit of 2×10^{-16} erg s^{-1} cm^{-2} in its wide survey (Euclid Collaboration: Mellier et al. 2024). On the contrary, photometric redshifts are obtained from multi-band wide filters instead of spectra so they can be measured for all the galaxies of the photometric sample. Despite their lower accuracy, they are now available for such a large number of galaxies that they can be used to put significant constraints on cosmology. One recent example is the latest results from the Dark Energy Survey (DES) which constrain the BAO shift parameter α with an uncertainty of 2.1% at $z_{eff} = 0.85$ (Abbott et al. 2024, DES Y6 from now on) with a sample of almost 16 million galaxies selected among over 300 million observed. To do so, a tomographic approach is typically used, dividing the full galaxy sample into redshift bins and measuring the angular correlation function or angular power spectrum in each bin. In DES Y6, six bins were defined between $0.6 < z_{ph} < 1.2$. In this context, the *Euclid* photometric survey can increase its constraining power by including its photometric sample for galaxy clustering studies in addition to weak lensing analyses. One advantage of *Euclid* is that it will provide numerous photometric redshifts (about 1.5×10^9) in a much larger redshift range than previously available, covering $0.2 < z_{ph} < 2.5$.

In this work, we study how well the *Euclid* photometric sample will be able to constrain the BAO scale, using the Flagship simulation (Euclid Collaboration: Castander et al. 2024). We consider two analyses, one in which we extract the BAO scale in each of the 13 redshift bins (Euclid Collaboration: Mellier et al. 2024), yielding 13 values of α and thus the evolution of the parameter as a function of redshift, and the second in which we conduct a joint analysis of all the redshift bins to constrain a single value of α. Here, we focus on the two-point angular correlation function in configuration space $w(\theta)$ as an observable to detect the BAO signal in the Flagship galaxy mock catalogue. While *Euclid* is expected to cover an area of about $14\,000$ deg^2 (Euclid Collaboration: Mellier et al. 2024), the Flagship simu-

---

lation covers 37% of this area. This means that the area used in this work is intermediate between Data Release 1 and 2 for *Euclid*, which are expected to cover approximately 2500 and 7500 deg^2, respectively. We want to quantify our ability to constrain this signal as well as estimate the weight of different choices in the setup of the analysis.

The paper is organized as follows. We describe the theoretical framework of the analysis in Sect. 2 with the computation of the two-point angular correlation function model, its estimator, and its covariance. The method used to extract the BAO scale and to infer cosmological parameters is detailed in Sect. 3. In Sect. 4, we present the data from the Flagship simulation used throughout this work. Results are reported and discussed in Sect. 5, including our joint analysis, the individual redshift bin analysis, and cosmological constraints along with their robustness to choices of fitting templates, scale cuts, redshift-space distortions (RSD), and redshift binning scheme. We present our main conclusions in Sect. 6.

2. Two-point angular correlation function

In this section we describe the observable relevant to galaxy clustering with the photometric survey that has been considered in this analysis: the galaxy two-point angular correlation function. We also present its estimator and its covariance.

2.1. Theory

As we process information projected into bins of redshift, we consider the galaxy two-point angular correlation function $w(\theta)$, defined as (e.g., Crocce et al. 2011)

$$w(\theta) = \sum_{\ell \geq 0} \frac{2\ell + 1}{4\pi} C(\ell) P_\ell(\cos\theta), \tag{1}$$

with P_ℓ being the Legendre polynomial and $C(\ell)$ the angular power spectrum defined as

$$C(\ell) = 4\pi \int_0^\infty \frac{\mathrm{d}k}{k} \mathcal{P}_\Phi(k) \Delta_\ell^2(k). \tag{2}$$

In Eq. (2), k is the wavenumber and $\mathcal{P}_\Phi$ stands for the dimensionless power spectrum of the primordial curvature perturbations $\Phi(k)$ that we model with HMCode (Mead et al. 2021) as implemented in the Boltzmann code CAMB (Challinor & Lewis 2011). The term Δ_ℓ is the sum of the transfer function of number counts for the galaxy density field Δ_ℓ^D and the linear RSD contribution Δ_ℓ^RSD (Chisari et al. 2019)

$$\Delta_\ell(k) = \Delta_\ell^\mathrm{D}(k) + \Delta_\ell^\mathrm{RSD}(k), \tag{3}$$

where the two terms are respectively defined as

$$\Delta_\ell^\mathrm{D}(k) := \int_0^{z_{max}} \mathrm{d}z \, p(z) \, b(z) \, T_\delta(k,z) \, j_\ell(kr) \tag{4}$$

and

$$\Delta_\ell^\mathrm{RSD}(k) := \int_0^{z_{max}} \mathrm{d}z \, \frac{(1+z) \, p(z)}{H(z)} T_\theta(k,z) \, j_\ell''(kr), \tag{5}$$

where $p(z)$ is the normalized galaxy redshift distribution, $b(z)$ is the linear galaxy bias, z_{max} is the maximum redshift of the survey that we fix to 3 for practical purposes, j_ℓ is the spherical Bessel function of order ℓ, j_ℓ'' its second derivative, and $r(z)$ is the comoving radial distance. In Eqs. (4) and (5), the transfer function

$T_\mathrm{X}(k,z)$ of a quantity X is defined as the ratio $X(k,z)/\Phi(k)$ so that T_δ is the transfer function of the matter overdensity $\delta(k,z)$ and T_θ is the transfer function of the divergence of the comoving velocity field. Discussed in Lepori et al. (2022) regarding full-shape analyses of photometric galaxy clustering, we checked that the effect of magnification bias over α is smaller than $0.2\,\sigma$ in most redshift bins, which is why no $\Delta_\ell^\mathrm{M}(k)$ term as defined in Eq. (26) of Chisari et al. (2019) is included in the model. Other relativistic effects are completely sub-dominant and not included either (Alonso et al. 2015).

To accurately model large scales at $\ell < 220$ needed for BAO analysis, non-Limber integrals are computed using the Fang–Krause–Eifler–MacCrann (FKEM) method described in Fang et al. (2020a), while the faster Limber approximation (Kaiser 1992) is used at $\ell \in [220, 10000]$. We checked that the effect of the Limber approximation over $C(\ell)$ is smaller than 1% in this range of ℓ. Throughout this work, the theoretical $w(\theta)$ is computed using the Core Cosmology Library (Chisari et al. 2019). We refer to $w_\mathrm{fid}(\theta)$ when the theoretical $w(\theta)$ is computed with the fiducial cosmological parameters defined in Sect. 4.1.

2.2. Estimator

The two-point angular correlation function is computed from the Flagship Mock Galaxy Catalogue (see Sect. 4) with the Landy–Szalay estimator (Landy & Szalay 1993)

$$w(\theta) = \frac{N_\mathrm{DD} - 2N_\mathrm{DR} + N_\mathrm{RR}}{N_\mathrm{RR}}, \tag{6}$$

where N_DD, N_DR, and N_RR are the pair counts where D stands for data and R for a random point. The random catalogues are created by sampling the footprint of the Flagship simulation defined by a HEALPix mask of $N_\mathrm{side} = 4096$, which is equivalent to an angular resolution of $0°.014$. We use 30 times as many random points as galaxies, yielding 1.04×10^9 points per redshift bin. The angular binning has a resolution of $0°.1$ and spans between $\theta_\mathrm{min} = 0°.12$ and $\theta_\mathrm{max} = \theta_\mathrm{BAO} + 2°.5$ where θ_BAO is

$$\theta_\mathrm{BAO} = \frac{r_\mathrm{s, drag, fid}}{(1 + z_\mathrm{eff}) \, D_\mathrm{A, fid}(z_\mathrm{eff})}, \tag{7}$$

evaluated at the mean redshift of the bin z_eff for the cosmology of the simulation given in Sect. 4.1. The measurement of $w(\theta)$ is performed with the code TreeCorr (Jarvis et al. 2004) and errors are estimated by a jackknife resampling of $N_\mathrm{patch} = 500$ patches of about $10\,\mathrm{deg}^2$ each.

2.3. Covariance

Two approaches are considered to compute the covariance of the two-point angular correlation function. For individual bin analyses, in which one value of the α parameter is fitted for each redshift bin, we use the jackknife covariance matrix built from the data vector measured with TreeCorr while joint analyses use an analytical covariance computed with CosmoCov (Krause & Eifler 2017). The use of an analytical covariance is made necessary by the noise in the covariance of the 13 redshift bins, even with 500 jackknife patches. Increasing to larger number of patches yields very little improvement in that regard.

The jackknife covariance matrix is computed with

$$\mathrm{Cov}^\mathrm{JK}(w_{ij}(\theta), w_{kl}(\theta'))$$

$$= \frac{N_\mathrm{patch} - 1}{N_\mathrm{patch}} \sum_{n=1}^{N_\mathrm{patch}} \left(w_{ij}^{(n)}(\theta) - \overline{w}_{ij}(\theta) \right)^\mathrm{T} \left(w_{kl}^{(n)}(\theta') - \overline{w}_{kl}(\theta') \right), \tag{8}$$

where n is the index of the jackknife realization, $w_{ij}(\theta)$ is the correlation of redshift bins i and j at angular separation θ, and $\overline{w}_{ij}$ stands for the mean over all jackknife realizations for each angular separation $\overline{w}_{ij}(\theta) = \frac{1}{N_{\text{patch}}} \sum_{n=1}^{N_{\text{patch}}} w_{ij}^{(n)}(\theta)$.

We checked that the jackknife covariance matrix of each individual redshift bin is numerically stable with conditioning numbers ranging from 2.3×10^4 for the covariance of the last redshift bin to 2.2×10^5 for the first bin. Multiplying each of the jackknife covariances by its inverse yields the identity matrix, as expected from a numerically stable matrix, with a ratio between the diagonal and off-diagonal terms larger than 10^{13}. In the MCMC analyses of Sect. 5, the inverse of the covariance is corrected by the Hartlap multiplicative factor defined in Hartlap et al. (2007)

$$\Psi = \frac{N_{\text{patch}} - N_{\text{b}} - 2}{N_{\text{patch}} - 1}, \tag{9}$$

where N_{b} is the number of angular bins in the data vector.

The analytical covariance used in Sect. 5.1 is the sum of the Gaussian and super-sample contributions, leaving aside the connected non-Gaussian term from modes within the footprint. The Gaussian term is computed using CosmoCov as in Krause & Eifler (2017) and Fang et al. (2020b), with a correction for the survey footprint like in Troxel et al. (2018) and without considering the Limber approximation (Fang et al. 2020a)

$$\text{Cov}^{\text{G}}\left(C_{ij}(\ell), C_{kl}(\ell')\right) = \frac{4\pi\,\delta_{\ell\ell'}^{\text{K}}}{\Omega_{\text{s}}\,(2\ell+1)} \left[\left(C_{ik}(\ell) + \frac{\delta_{ik}^{\text{K}}}{\bar{n}_i}\right)\right.$$
$$\left. \times \left(C_{jl}(\ell') + \frac{\delta_{jl}^{\text{K}}}{\bar{n}_j}\right) + \left(C_{il}(\ell) + \frac{\delta_{il}^{\text{K}}}{\bar{n}_i}\right)\left(C_{jk}(\ell') + \frac{\delta_{jk}^{\text{K}}}{\bar{n}_j}\right)\right], \tag{10}$$

with C_{ij} the angular power spectrum of redshift bins i and j, Ω_{s} the survey area, $\bar{n}$ the effective number density of galaxies and i, j, k, and l are the indices of the redshift bins. The two-point angular correlation function is then computed from angular power spectra with (Abbott et al. 2024)

$$\text{Cov}^{\text{G}}\left(w_{ij}(\theta), w_{kl}(\theta')\right)$$
$$= \sum_{\ell,\ell'} \frac{(2\ell+1)(2\ell'+1)}{(4\pi)^2} \overline{P_\ell}(\theta)\,\overline{P_{\ell'}}(\theta')\,\text{Cov}^{\text{G}}\left(C_{ij}(\ell), C_{kl}(\ell')\right), \tag{11}$$

with $\overline{P_\ell}$ the Legendre polynomial averaged over angular bins

$$\overline{P_\ell} := \frac{\int_{x_{\text{min}}}^{x_{\text{max}}} \mathrm{d}x\, P_\ell(x)}{x_{\text{max}} - x_{\text{min}}} = \frac{[P_{\ell+1}(x) - P_{\ell-1}(x)]_{x_{\text{min}}}^{x_{\text{max}}}}{(2\ell+1)(x_{\text{max}} - x_{\text{min}})} \tag{12}$$

in which $x = \cos(\theta)$ with $\theta_{\text{min}}, \theta_{\text{max}}$ the lower and upper limits of each angular bin.

As for the super-sample covariance (SSC) contribution to the covariance, it was computed following the fast approximation from Lacasa & Grain (2019) extended to partial-sky in Gouyou Beauchamps et al. (2022) to go beyond the full-sky approximation by taking into account the footprint of the survey

$$\text{Cov}^{\text{SSC}}\left(w_{ij}(\theta), w_{kl}(\theta')\right) \approx \tilde{w}_{ij}(\theta)\,\tilde{w}_{kl}(\theta')\,S_{ijkl}, \tag{13}$$

where $\tilde{w}_{ij}(\theta)$ is computed as

$$\tilde{w}_{ij}(\theta) = \sum_\ell \frac{2\ell+1}{4\pi}\,R_\ell\,C_{ij}(\ell)\,P_\ell(\cos\theta) =: (R * w_{ij})(\theta), \tag{14}$$

with R_ℓ the response of the galaxy power spectrum to variations of the background density $\frac{\partial P_{\text{gal}}(k,z)}{\partial \delta_{\text{b}}}$. The S_{ijkl} matrix element is computed using the implementation from PySSC [1] as

$$S_{ijkl} = \int \mathrm{d}V_1\,\mathrm{d}V_2\, \frac{W_i(z_1)\,W_j(z_1)\,W_k(z_2)\,W_l(z_2)\,\sigma^2(z_1, z_2)}{\int \mathrm{d}V_1\,W_i(z_1)\,W_j(z_1) \int \mathrm{d}V_2\,W_k(z_2)\,W_l(z_2)}, \tag{15}$$

where W_i is the kernel of the observable in redshift bin i, the kernel being the normalized redshift distribution $p_i(z)$ in the case of photometric galaxy clustering. The comoving volume element $\mathrm{d}V = r^2(z)\,(\mathrm{d}r/\mathrm{d}z)\,\mathrm{d}z$ is integrated between $z = 0$ and $z = z_{\text{max}} = 3$. The variance of the background density σ^2 is, for a survey with a window function $\mathcal{W}$ of angular power spectrum $C^{\mathcal{W}}$

$$\sigma^2(z_1, z_2) = \frac{1}{\Omega_{\text{s}}^2} \sum_\ell (2\ell+1)\,C^{\mathcal{W}}(\ell)\,C(\ell, z_1, z_2), \tag{16}$$

where the angular matter power spectrum between redshifts z_1 and z_2 is obtained from the 3D matter cross-spectrum $P_{\text{m}}(k\,|\,z_{12}) = D(z_1)\,D(z_2)\,P_{\text{m}}(k, z = 0)$ with

$$C(\ell, z_1, z_2) = \frac{2}{\pi} \int_{k_{\text{min}}}^{k_{\text{max}}} k^2\,\mathrm{d}k\, P_{\text{m}}(k\,|\,z_{12})\,j_\ell(kr_1)\,j_\ell(kr_2), \tag{17}$$

where $D(z)$ is the linear growth factor, $r_i = r(z_i)$ is the comoving radial distance, $k_{\text{min}} = 0.1/r(z_{\text{max}})$, and $k_{\text{max}} = 10/r(z_{\text{min}})$.

We use the anafast routine from the HEALPix [2] library (Zonca et al. 2019; Górski et al. 2005) to compute $C^{\mathcal{W}}$. We make the approximation of a constant $R_\ell = 5$, which reduces the convolution product to a multiplication. A detailed discussion on the response of the SSC can be found in Euclid Collaboration : Sciotti et al. (2024). The approximation on R_ℓ used in this work has an impact which does not exceed 0.5% on α and 3% on its uncertainty in all redshift bins, which is expected given the angular scales and redshifts considered.

3. Methodology

3.1. Galaxy bias

A fit of the linear galaxy bias $b(z)$ is performed in each redshift bin using the jackknife covariance and the residuals $w(\theta) - b^2 w_{\text{fid},b=1}(\theta)$, where $w_{\text{fid},b=1}$ denotes the theoretical angular correlation function defined in Eq. (1) computed with the Flagship cosmology and a galaxy bias $b = 1$. We use scales between $0°\!.5$ and $4°$ in this full shape fit. A third order polynomial is then fitted to the result

$$b(z) = b_3 z^3 + b_2 z^2 + b_1 z + b_0, \tag{18}$$

which is then used in Eq. (4) to compute the theoretical model of the two-point angular correlation function.

3.2. BAO template-fitting

To extract the BAO feature from the photometric sample, we perform the fitting between the measured $w(\theta)$ and a template derived from the theoretical two-point angular correlation function $w_{\text{fid}}(\theta)$ computed for the fiducial cosmology described in Sect. 4.1. The template is defined as

$$T(\alpha, \theta) := B\,w_{\text{fid}}(\alpha\theta) + A_0 + \frac{A_1}{\theta} + \frac{A_2}{\theta^2}, \tag{19}$$

---

[1] https://github.com/fabienlacasa/PySSC
[2] http://healpix.sf.net

Table 1. Priors used for the template-fitting parameters. With the first template, defined in Eq. (19), the A_i parameters have a unit of deg^i. For the other templates, defined in Sect. 5.5, the units should be adapted to have a template $T(\alpha, \theta)$ of unit consistent with $w(\theta)$.

α	$10^3 A_0$	$10^3 A_i \ (i \neq 0)$	B
$[0.8, 1.2]$	$[-1, 1]$	$[-5, 5]$	$[0.2, 6]$

where α is the transverse Alcock–Paczynski parameter quantifying an eventual shift of the BAO peak between the measured $w(\theta)$ and the fiducial $w_{\rm fid}(\theta)$. The nuisance parameters B, A_0, A_1, and A_2 are needed to absorb residual effects like non-linear galaxy bias. Different template parametrisations can be used and we will verify in Sect. 5.5 that the choice of polynomial has minimal impact on the α parameter. The parameter of interest in this work is α and, since the fiducial cosmology used to compute $w_{\rm fid}(\theta)$ is the same as the simulation, we expect to recover $\alpha = 1$. On the contrary, using a different fiducial cosmology to compute $w_{\rm fid}(\theta)$ should result in $\alpha \neq 1$.

We will consider one set of nuisance parameters per redshift bin, since these parameters can in principle vary with redshift. This represents a total of 53 parameters for the joint analysis and 5 parameters for the analysis of each of the 13 bins. The Markov Chain Monte-Carlo (MCMC) technique is used to quantify the uncertainty on α marginalised over the nuisance parameters. The `emcee` sampler introduced in Foreman-Mackey et al. (2013) is used with the Gelman–Rubin convergence stopping criterion described in Gelman & Rubin (1992) with a threshold $R_{\rm GR} - 1 = 0.005$ for analyses on individual redshift bins and $R_{\rm GR} - 1 = 0.02$ for joint analyses. These thresholds were chosen to stop chains when parameter values and uncertainties reached a plateau. Uniform priors applied to the template parameters are presented in Table 1.

As a comparison to MCMC, we also consider the frequentist approach of profile likelihood to provide constraints in the joint analysis. We obtain the profile likelihood $\Delta\chi^2(\alpha) = \chi^2(\alpha) - \chi^2(\alpha)\big|_{\rm min}$ by computing the best fit χ^2 for each value of α between 0.8 and 1.2 in steps of 0.001. We then fit an 8th-order polynomial to this profile to compute $\Delta\chi^2$. The 1σ uncertainty on α is then given by $\Delta\chi^2 = 1$. In the joint analysis, the resolution of the grid of α on which this polynomial is evaluated is increased to use steps of 0.0001 to match the increased constraining power. We also use this frequentist approach to quantify the significance of the BAO detection as described in Sect. 5.1. The code `iminuit` based on the MINUIT algorithm is used at this effect (Dembinski et al. 2020; James & Roos 1975).

3.3. Cosmological parameters

Extracting the transverse Alcock–Paczynski α parameter in successive tomographic bins of redshift allows us to constrain the evolution of the expansion of the Universe. Indeed, the α parameter can be expressed as

$$\alpha = \frac{D_{\rm A}}{r_{\rm s, drag}} \frac{r_{\rm s, drag, fid}}{D_{\rm A, fid}}, \tag{20}$$

where $D_{\rm A}$ is the angular diameter distance, $r_{\rm s, drag}$ corresponds to the sound horizon at the drag epoch, and the fid label stands for the values in the fiducial cosmology. The detail of the computation of $r_{\rm s, drag}$ can be found in Appendix A. Since α depends on H_0, $\omega_{\rm b} = \Omega_{\rm b} h^2$, and $\omega_{\rm cdm} = (\Omega_{\rm m} - \Omega_{\rm b}) h^2$, these cosmological parameters can be constrained with MCMC by comparing the α_i value for each redshift bin to the theoretical expected value
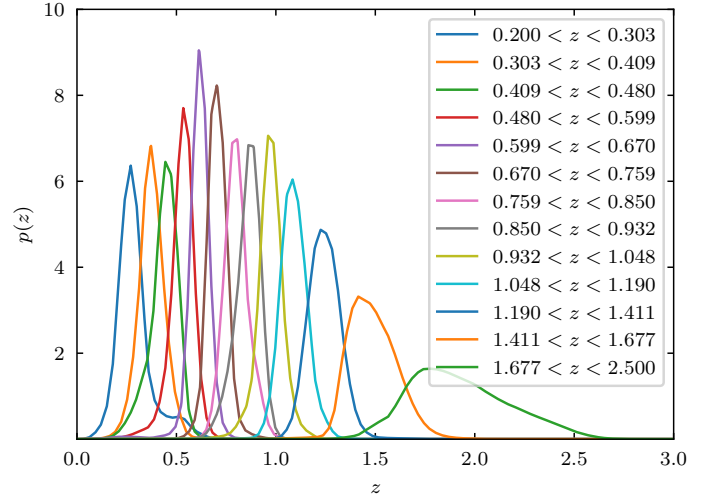
Fig. 1. True redshift distribution of the galaxies from Flagship 2.1.10 selected in 13 equipopulated photometric redshift bins.

for the fiducial cosmology of the simulation. We note that we neglect the mass of neutrinos and consider that all the matter is given by the sum of cold dark matter and baryonic matter, for simplicity. In Eq. (20), the respective quantities are all evaluated at the effective redshift. The effective redshift of bin i is defined as

$$z_{\rm eff, i} := \int_0^{z_{\rm max}} {\rm d}z \, z \, p_i(z), \tag{21}$$

where $p_i(z)$ is the normalized distribution of photometric redshifts shown in Fig. 1. We checked that using the median redshift of each redshift bin did not affect the constraints on H_0, $\Omega_{\rm b}$, and $\Omega_{\rm cdm}$ (shift smaller than $0.03\,\sigma$).

We use Gaussian priors from *Planck* (Ade et al. 2016) adapted to match the Flagship simulation cosmological parameters so that the ratios between the uncertainties and fiducial values stay the same, yielding $\omega_{\rm b} = 0.02200 \pm 0.00036$ and $D_{\rm A}(1 + z_{Planck})/r_{\rm s, drag} = 83.197 \pm 0.065$ with $z_{Planck} = 1090$.

4. Data

4.1. Euclid Flagship simulation

We use the Flagship v.2.1.10 galaxy mock sample (Euclid Collaboration: Castander et al. 2024) available to the Euclid Consortium on CosmoHub [3] (Tallada et al. 2020; Carretero et al. 2017) created from the Flagship N-body dark matter simulation (Potter et al. 2017). This simulation assumes the following flat ΛCDM cosmology: matter density parameter $\Omega_{\rm m} = 0.319$, baryon density parameter $\Omega_{\rm b} = 0.049$, dark energy density parameter $\Omega_\Lambda = 0.681 - \Omega_{\rm r} - \Omega_\nu$, with a radiation density parameter $\Omega_{\rm r} = 0.00005509$ and $\Omega_\nu = 0.00140343$ for massive neutrinos, dark energy equation of state parameter $w_{\rm de} = -1.0$, reduced Hubble constant $h = 0.67$, spectral index of the primordial power spectrum $n_{\rm s} = 0.96$, and its amplitude $A_{\rm s} = 2.1 \times 10^{-9}$ at $k = 0.05\,{\rm Mpc}^{-1}$. This simulation considers a $3.6\,h^{-1}$ Gpc-side box with 4×10^{12} particles of mass $10^9\,h^{-1} M_\odot$. The main output of the simulation is a lightcone that spans redshifts between 0 and 3. Dark matter haloes are identified down to $10^{10}\,h^{-1}\,M_\odot$ with `ROCKSTAR` (Behroozi et al. 2013). These haloes are then populated with galaxies with halo abundance matching and halo

---

[3] https://cosmohub.pic.es/
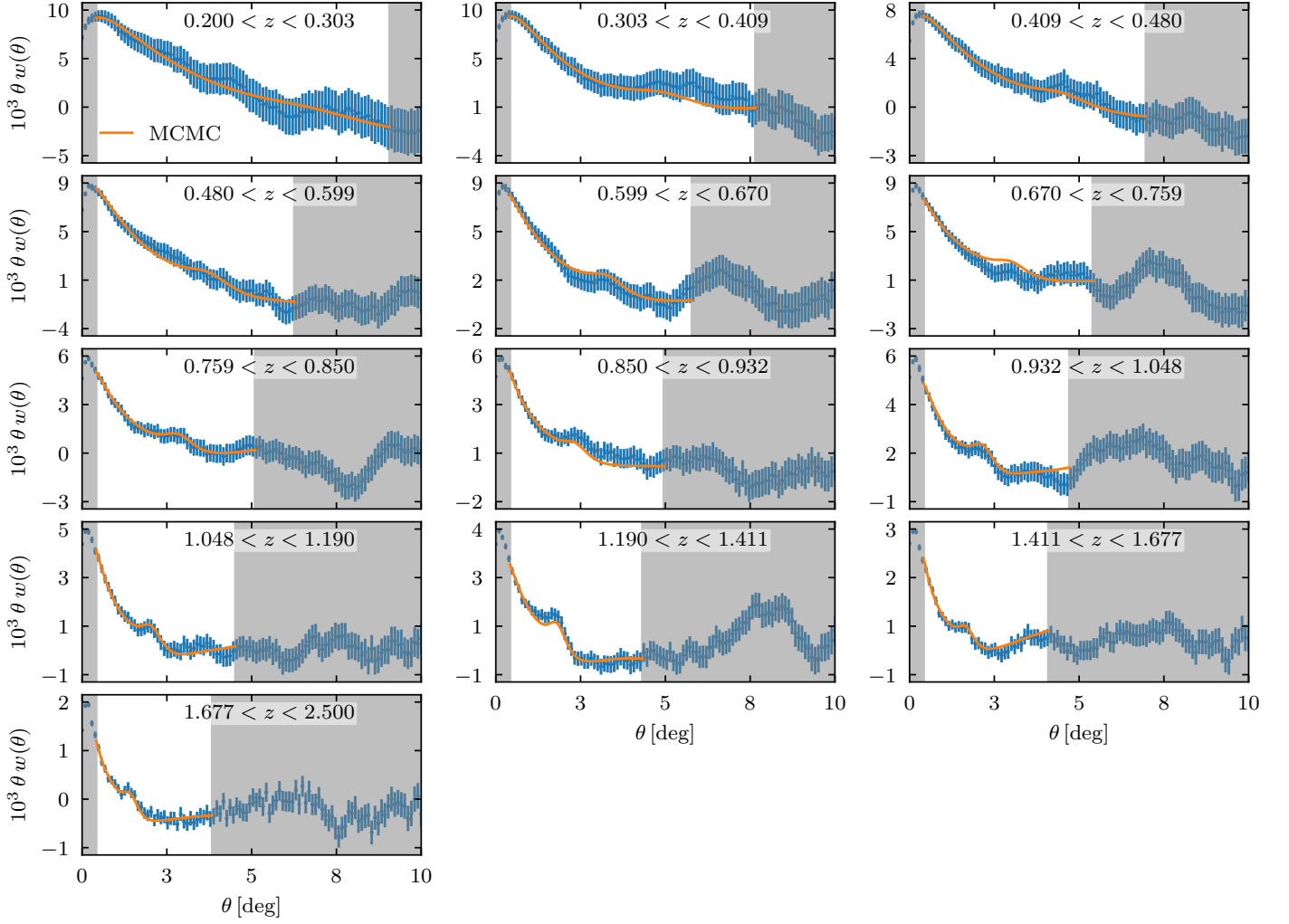
Fig. 2. Two-point angular correlation function measured on the Flagship simulation in 13 redshift bins. The errors come from the analytical covariance presented in Sect. 2.3. The orange curve is the correlation function computed using the template from Eq.(19) evaluated with the parameters inferred from MCMC in each redshift bin. Scale cuts are shown as grey bands and are defined as $\theta_{min} = 0°6$, $\theta_{max} = \theta_{BAO} + 2°5$ where θ_{BAO} is the expected position of the BAO peak in the fiducial cosmology.

occupation distribution techniques following Carretero et al. (2015). Galaxy luminosities have been calibrated with a combination of the luminosity functions from Blanton et al. (2003), Blanton et al. (2005a), and Dahlen et al. (2005). Galaxy clustering measurements have been calibrated as a function of colour and luminosity following Zehavi et al. (2011) and the colour-magnitude diagram from Blanton et al. (2005b) has been used as a reference.

We apply a magnitude cut at $I_E \leq 24.5$ in the VIS I_E band with the additional constraint that only objects with properly determined photometric redshifts are considered (`phz_flags = 0`). This sample covers one octant of the sky between right ascension $145° \leq RA < 235°$ and declination $0° < Dec < 90°$ for a total area of 5157 deg². Following Euclid Collaboration: Mellier et al. (2024), we divide the sample into 13 equipopulated redshift bins of z_{ph}. The normalized redshift distributions $p_i(z)$ of the 13 bins are shown in Fig. 1. This division yields a large statistic sample, with about 34.8 million galaxies per redshift bin. Photometric redshifts are defined as the first mode of the probability density functions (PDF) obtained with the k-nearest neighbours algorithm NNPZ (Tanaka et al. 2018) by matching galaxy magnitude and colours to a reference sample of 2 million galaxies simulated up to the depth of the *Euclid* calibration field

$I_E = 29.4$ and whose PDF are obtained using the template-fitting code `Phosphoros` (Tucci et al., in prep). The photometric redshift PDF of each galaxy is computed as a weighted average of the PDF of the neighbours found by NNPZ, the weight being the inverse of the χ^2 distance between the galaxy and the neighbour in the magnitude and colour space. The constraint `phz_flags = 0` ensures that the galaxy had enough neighbours found to properly derive the photometric redshift when NNPZ was applied. The photometry used to infer these redshifts has the quality expected from the ground-based observations of the Legacy Survey of Space and Time (LSST, Ivezić et al. 2019) for all galaxies which is optimistic.

The fiducial cosmology used in this paper is a flat ΛCDM cosmology, defined by a set of parameters which match the fiducial cosmology of the Flagship simulation.
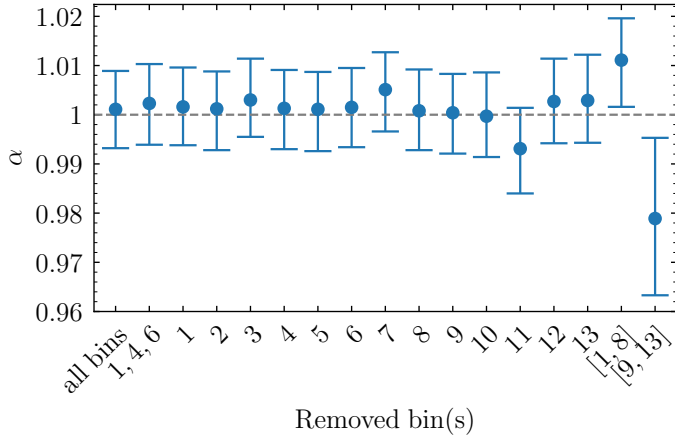
5. Results

5.1. Joint BAO measurement

In this section, we present the constraints on α obtained with a joint analysis of the 13 redshift bins. We used the template as defined in Sect. 3.2 extended to have bin-specific nuisance
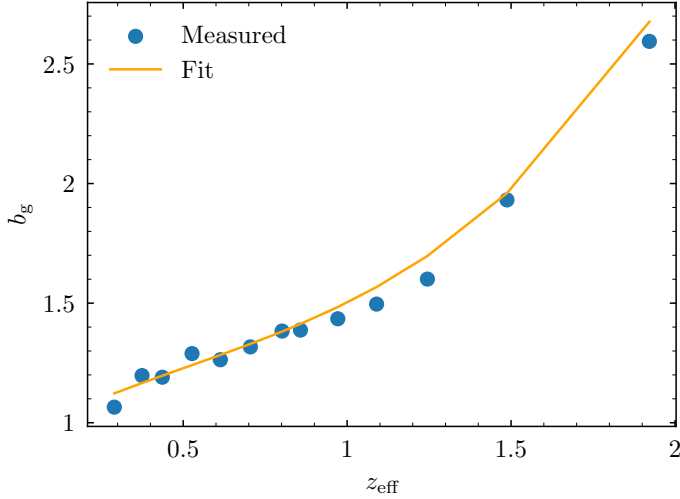
Fig. 3. Galaxy bias measured on Flagship 2.1 between $0°5$ and $4°0$ and its polynomial fit.

Fig. 4. Comparison of α from a joint analysis in which redshift bins are successively removed. Bin 11 with effective redshift $z_{eff} = 1.245$ has a larger effect over the joint constraints compared to other bins, as one can see from the shift and increase of the uncertainty when it is not included. Selecting high- or low-redshift bins respectively induces a 1.3 or 2.8 $\sigma_{all\,bins}$ shift towards higher or lower values for α.

parameters B_i, $A_{0,i}$, $A_{1,i}$, and $A_{2,i}$ with $i \in [1, 13]$. Scale cuts are $\theta_{min} = 0°6$, $\theta_{max} = \theta_{BAO} + 2°5$, visible as grey bands in Fig. 2 and discussed in detail in Sect. 5.6. We clearly see that the position of the BAO peak is found at lower angles as redshift increases, varying from $7°$ in the first redshift bin to $1°6$ in the last one. We will study the impact of a different choice of scale cuts in Sect. 5.6. We use the analytical covariance (Gaussian and SSC) for this joint analysis.

We first report the estimate of the linear galaxy bias, shown in Fig. 3 with the best fit obtained for $b_3 = 0.2681$, $b_2 = -0.4090$, $b_1 = 0.6944$, and $b_0 = 0.9493$ as the coefficients of Eq. (18). These values of the bias coefficients are then used to compute the fiducial $w_{fid}(\theta)$ that will be injected in the template of Eq. (19). Eventual non-linearities of the galaxy bias at small scales or systematic effects are absorbed by the template nuisance parameters without affecting α, our parameter of interest.

For this joint analysis with all redshift bins, we report a constraint of $\alpha = 1.0011^{+0.0078}_{-0.0079}$, obtained with a profile likelihood approach (Ade et al. 2014). This approach consists in minimizing the χ^2 while fixing a parameter at various values to obtain a

profile of χ^2 as a function of this parameter. Repeating this with another model of $w(\theta)$, we can then obtain the difference of the profiles $\Delta\chi^2$. This result might seem optimistic given that it represents an improvement by a factor of 3 with respect to the latest results from the DES Y6 analysis which yield a constraint of α at the 2.4% level with the angular two-point correlation function. However, several factors need to be taken into account in this comparison. The first one is that this work uses data from a simulation and so it is inherently optimistic since it is free from systematic effects while DES Y6 uses real observations and has to correct them. In DES Y6, 5 redshift bins between $0.7 < z < 1.2$ are used whereas the Flagship sample is here divided into 13 redshift bins between $0.2 < z < 2.5$, which increases significantly the constraining power of the joint analysis. We define the significance of the BAO detection to be

$$\Delta_{det} := \left| \chi^2_w(\alpha_{min}) - \chi^2_{no\,wiggle}(\alpha_{min}) \right|^{1/2} , \qquad (22)$$

evaluated at the α_{min} value minimizing $\chi^2_w(\alpha)$. The $\chi^2_{no\,wiggle}$ is computed using the transfer function from Eisenstein & Hu (1998) in which the BAO wiggles have been removed, unlike the transfer function from CAMB (Lewis et al. 2000) used to obtain χ^2_w. We quantified $\Delta_{det} = 10.3\,\sigma$ with a profile likelihood approach with our data compared to $3.5\,\sigma$ in DES Y6. We also find significantly tighter constraints in each individual redshift bin, contributing to this result.

For this joint analysis, we find that the results obtained with profile likelihood and MCMC differ significantly because of the combined effect of the strong constraining power and the disagreement between the preferred values of α in different redshift bins. This leads to a poor exploration of a multi-modal posterior. In more detail, the analytical covariance yields $\alpha = 0.9997^{+0.0003}_{-0.0002}$ with the MCMC analysis, while considering only the diagonal of the analytical covariance results in $\alpha = 1.0096^{+0.0085}_{-0.0087}$. As a comparison, when we only consider the diagonal of the jackknife covariance, we find $\alpha = 1.0095^{+0.0108}_{-0.0108}$, which corresponds to a 27% increase of the uncertainty explained by the larger amplitude of the jackknife errors. The results that we obtain from a profile likelihood approach with or without the off-diagonal terms of the analytical covariance are instead similar, with a $1\,\sigma$ uncertainty of ± 0.0079 and ± 0.0097, respectively.

We further investigate this result by using a similar approach to DES Y6 by excluding redshift bins in which the BAO signal is not detected with sufficient strength. In this case, Δ_{det} is computed for each individual redshift bin and a non-detection is then defined as a detection level $\Delta_{det} < 1$. A non-detection in the first bin ($0.6 < z < 0.7$) is why 5 bins were used in the analysis of DES Y6 instead of 6. After excluding the redshift bins with no significant detection (bins 1, 4, and 6), we report a value $\alpha = 1.0023^{+0.0080}_{-0.0084}$, almost identical to the result obtained when including all the redshift bins. The fact that the increase of the uncertainty is as small as 4.5% despite removing three out of 13 bins can be understood by the fact that if redshift bins have no significant detection of the BAO signal then they provide very little constraining power on α. We check the robustness of our result with respect to all the redshift bins included in the joint analysis in Sect. 5.2.

An important caveat to fitting a unique α to all redshift bins is that it assumes a perfect match between the fiducial cosmology and the true cosmology of the Universe which is unknown. Any mismatch will lead to a variation of α which depends on redshift. This effect can be quantified thanks to the definition of α in Eq. (20) in which D_A and $r_{s,drag}$ are computed for different cosmologies while $D_{A,fid}$ and $r_{s,drag,fid}$ are
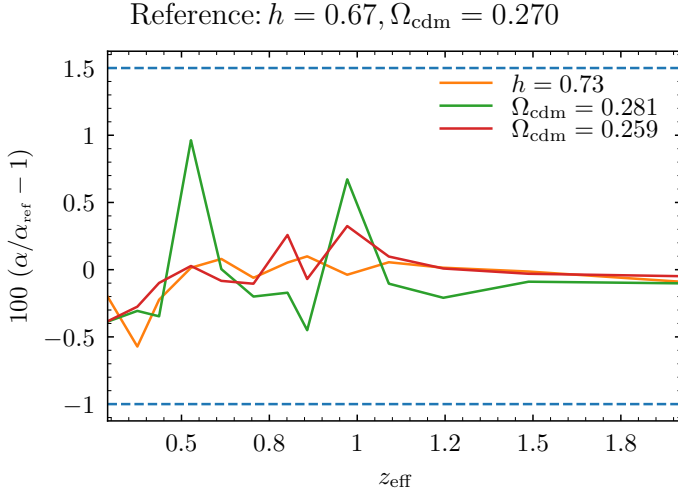
Fig. 5. Effect of the fiducial cosmology on α in all redshift bins for three variations replacing $h = 0.67$ by $h = 0.73$ and $\Omega_{cdm} = 0.270$ by $\Omega_{cdm} = 0.281$ or $\Omega_{cdm} = 0.259$. The dashed line shows a relative difference of 1%. The effect of the fiducial cosmology is negligible with respect to the uncertainties varying between ± 0.13 and ± 0.024.

constant at the fiducial cosmology of the Flagship simulation. We check that varying Ω_{cdm}, Ω_b, and h by 5% leads to a maximum expected variation of α of 1% between the first and last redshift bin. This maximum variation of α scales linearly as $\alpha(z_{eff} = 1.922)/\alpha(z_{eff} = 0.290) \propto 0.2\,\Delta(\Omega_{cdm}, \Omega_b, h)$. Given the constraint obtained on α, this effect is non-negligible and is a limit to this joint analysis. For this reason, the analysis is also performed in individual redshift bins in Sect. 5.3.

5.2. Robustness validation

In this section, the impact of the different redshift bins in the joint analysis is evaluated by removing each of the 13 redshift bins, one at a time. The constraints on α for all these cases are shown in Fig. 4. While most bins have very little effect over the constraints, removing the redshift bin 11 at $z_{eff} = 1.245$ from the joint analysis decreases α by $1\,\sigma_{all\ bins}$. It also increases uncertainties by 11%, which is expected given that we remove one of the redshift bin with the most constraining power. This constraining power can be understood by studying the properties of the photometric redshifts computed for the Flagship galaxy mock catalogue. Indeed, comparing them to the true redshifts of the simulation using the same binning, we find that with a measure of the scatter σ_{NMAD} robust to outliers and defined as

$$\sigma_{NMAD} = 1.4826\ \mathrm{median}\left(\frac{\Delta z - \mathrm{median}(\Delta z)}{1 + z_{true}}\right) \quad (23)$$

where $\Delta z = z_{ph} - z_{true}$, bin 11 has a scatter which is about 25% smaller than bins 12 and 13. The combination of good photometric redshifts and high redshift explains the importance of this bin.

If we compare constraints from bins with redshift $z_{eff} < 0.9$ to the baseline with all bins, we find that α is shifted by $2.8\,\sigma_{all\ bins}$ towards smaller values and its uncertainty is increased by a factor of two. On the contrary, including high-redshift bins $z_{eff} > 0.9$ and removing low-redshift bins, the shift towards a larger value of α is limited to $1.3\,\sigma_{all\ bins}$. The uncertainty is only increased by 14.6%, in this case. These results can be understood in light of the constraints from individual bins detailed in Table 2. Bins at $z_{eff} < 0.9$ with the largest level of sig-

Table 2. Values of α extracted from the MCMC analysis in each of the 13 redshift bins. The detection level is defined in Eq. (22). When the significance is smaller than $1\,\sigma$, the result is considered as a non-detection.

Bin	z_{eff}	α	$\Delta_{det}\ (\sigma)$
1	0.290	$1.026^{+0.122}_{-0.140}$	no detection
2	0.374	$1.044^{+0.097}_{-0.107}$	1.2
3	0.436	$0.957^{+0.112}_{-0.093}$	1.1
4	0.527	$1.003^{+0.146}_{-0.123}$	no detection
5	0.613	$1.002^{+0.079}_{-0.095}$	1.1
6	0.705	$0.985^{+0.087}_{-0.096}$	no detection
7	0.802	$0.932^{+0.072}_{-0.054}$	1.5
8	0.858	$1.052^{+0.067}_{-0.067}$	1.7
9	0.972	$1.037^{+0.057}_{-0.048}$	1.5
10	1.090	$1.015^{+0.029}_{-0.028}$	2.7
11	1.245	$1.031^{+0.024}_{-0.024}$	4.0
12	1.488	$0.996^{+0.040}_{-0.038}$	2.4
13	1.922	$0.991^{+0.036}_{-0.037}$	2.9

nificance of BAO detection are biased towards low values of α_i, which explains why the joint value of α increases when they are removed. On the other hand, bins at $z_{eff} > 0.9$ are overall biased towards larger values of α_i, which explains why removing them decreases the value of the joint α. The large difference in the uncertainty values for these last two cases (1.3 against $2.8\,\sigma_{all\ bins}$), can be explained by the much tighter constraints obtained at high redshift, where the BAO peak is not smeared.

5.3. Individual bins BAO measurement

The template fit is now applied to one redshift bin at a time, yielding 13 values of the α parameter. This reduces the constraining power over each α but gives information about the redshift evolution which can be used to constrain cosmological parameters as explained in Sect. 3.3. It is also a more relevant analysis in our setup given the caveat of fitting a unique α explained at the end of Sect. 5.1.

Table 2 groups the results for α in all 13 redshift bins, along with the associated sigma level of BAO detection. We first notice that the $1\,\sigma$ uncertainty is larger at low redshift. This is due to the smearing of the BAO signal by the non-linear evolution of the large-scale structures under the effect of gravitation. This is clearly visible in Fig. 2 where the BAO is much more peaked at higher redshift. The parameter α is compatible with $\alpha = 1$ within $1\,\sigma$ in all redshift bins with the exception of bin 11 at $z_{eff} = 1.245$ for which we find a $1.3\,\sigma$ shift. This bin is also the one with the strongest constraining power, explained by the high redshift and small scatter of photometric redshifts $\sigma_{NMAD} = 0.024$. As for the level of detection of the BAO signal, we find three redshift bins with no significant detection, bins 1, 4, and 6. Otherwise, the significance of the detections ranges between 1.1 and $4.0\,\sigma$ detections, with a maximum at $z_{eff} = 1.245$ and the $1\,\sigma$ uncertainty on α decreases as the detection level increases, as expected.

Table 3. Values of α extracted from the MCMC analysis in a DR1-like setting in each equidistant redshift bin. The detection level Δ_{det} is defined in Eq. (22).

Bin	z_{min}	z_{eff}	z_{max}	α	Δ_{det} (σ)
1	0.200	0.307	0.396	$1.055^{+0.102}_{-0.148}$	no detection
2	0.396	0.432	0.507	$1.021^{+0.118}_{-0.131}$	no detection
3	0.507	0.578	0.657	$1.086^{+0.068}_{-0.106}$	1.2
4	0.657	0.727	0.840	$0.909^{+0.113}_{-0.070}$	1.2
5	0.840	0.893	1.040	$1.016^{+0.120}_{-0.155}$	no detection
6	1.040	1.325	2.500	$1.045^{+0.079}_{-0.089}$	1.1

When averaged over all redshift bins, the shift between the results obtained with the jackknife and with the analytical co-variances is smaller than $0.3\,\sigma$ with the measured data vector and $0.08\,\sigma$ with a noise-free synthetic data vector computed like the theoretical model.

The impact of the choice of fiducial cosmology is investigated by varying h from 0.67 to 0.73. Galaxy bias is fitted again before repeating the MCMC analysis bin by bin. We expect a shift of α by a factor

$$\frac{D_{\mathrm{A}}(h=0.73, \Omega_{\mathrm{b}}, \Omega_{\mathrm{cdm}})}{r_{\mathrm{s,\,drag}}(h=0.73, \Omega_{\mathrm{b}}, \Omega_{\mathrm{cdm}})} \frac{r_{\mathrm{s,\,drag}}(h=0.67, \Omega_{\mathrm{b}}, \Omega_{\mathrm{cdm}})}{D_{\mathrm{A}}(h=0.67, \Omega_{\mathrm{b}}, \Omega_{\mathrm{cdm}})} = 0.982 \, .$$

(24)

After correction by this shift, we measure a remaining maximum relative difference $|\Delta\alpha|/\alpha$ of 0.01, the average over all redshift bins being 0.0012. This is illustrated in Fig. 5. As an additional test, we vary Ω_{cdm} by $\pm 5\,\sigma_{Planck}$, keeping $h = 0.67$ and $\Omega_{\mathrm{b}} = 0.049$. With $\Omega_{\mathrm{cdm}} = 0.281$ and $\Omega_{\mathrm{cdm}} = 0.259$, we respectively find a remaining maximum relative difference $|\Delta\alpha|/\alpha$ of 0.9% and 0.4%, the average over all redshift bins being 0.31% and 0.13%. These variations are negligible compared to the uncertainties on α, which shows that the analysis is robust against the choice of fiducial cosmology.

We also provide constraints in a DR1-like setting with a sample divided into 6 redshift bins, a selection cut at $I_{\mathrm{E}} \leq 23.5$, and covering 2500 deg^2. The measurement of $w(\theta)$ and BAO analysis were done following the same procedure. In this case, we find that the constraints on α in bins 1 to 6 are listed in Table 3.

These constraints are in agreement with $\alpha = 1$ within $1\,\sigma$. If we compare bins of similar effective redshifts, the constraints are about 20% weaker than with 13 bins in the first bins and significantly worse in the last two bins. The detection of the BAO signal is overall weaker than with 13 redshift bins, with no significant detection in bins 1, 2, and 5 and with $\Delta_{\mathrm{det}} \leq 1.2$ in the other bins. These results are expected from the larger uncertainties on $w(\theta)$ and the larger bins : intra-bin variations of the BAO scale dilute the signal. Note that the LSST-like photometry assumed to infer photometric redshifts is even more optimistic for this setting than for the previous one, since this photometry will not be available at the time of this data release. Instead, photometry from the Dark Energy Survey will be used (Abbott et al. 2018). For this reason, the fact that the redshift distribution $p(z)$ is well known is only true with the Flagship simulation. With data, calibrating the $p(z)$ bias and stretch prior to the analysis will be mandatory, as in Abbott et al. (2024). Ideally, these nuisance parameters for the bias and stretch of $p(z)$ will be marginalized
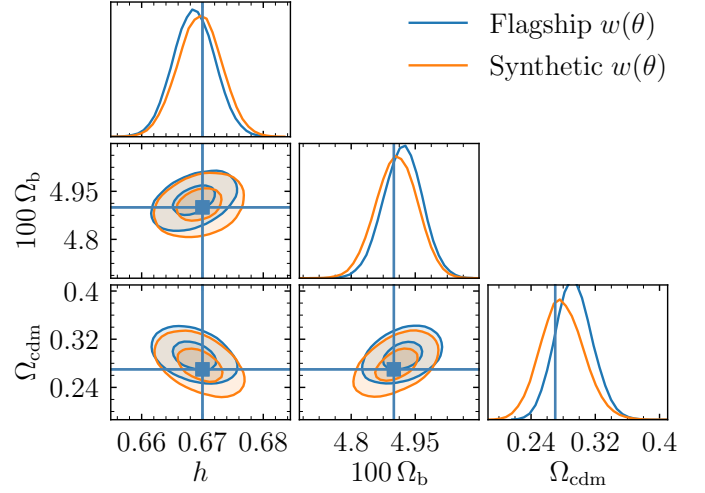

Fig. 6. Constraints on h, Ω_{b}, and Ω_{cdm} from BAO with *Planck* priors. The use of α_i derived from a synthetic two-point angular correlation function allows us to check that the biases observed with the measured data vector and shown in blue are decreased, by a factor of 3 for the largest one, on Ω_{cdm}.

over in the MCMC analysis of DR1 data as in Bertmann et al., in prep. These constraints could probably be improved with analysis choices tailored to this sample, for example with different scale cuts.

5.4. Cosmological constraints from BAO

One can constrain the h, Ω_{b}, and Ω_{cdm} parameters by sampling them in their dependence with respect to the values of α_i, $i \in [1, 13]$ (Eq. (20) and Appendix A) obtained by template fitting in each individual bin. We list in Table 2 the values of α_i and the associated uncertainties obtained by MCMC analysis. In Fig. 6, we show the constraints on h, Ω_{b}, and Ω_{cdm}. We obtain $h = 0.669 \pm 0.003$, $100\,\Omega_{\mathrm{b}} = 4.921^{+0.044}_{-0.046}$, and $\Omega_{\mathrm{cdm}} = 0.293^{+0.023}_{-0.022}$, which is in agreement with the simulation cosmology. Using the synthetic data vector instead of the measured two-point angular correlation function to extract the α_i and then obtain cosmological constraints with the same analysis, we check that the bias on Ω_{cdm} decreases from $1\,\sigma$ to $0.3\,\sigma$.

We check how excluding one or some redshift bins from this analysis affects the cosmological constraints. Figure 7 groups all results for h, Ω_{b}, and Ω_{cdm} with *Planck* priors. We consider the α_i, $i \in [1, 13]$ obtained by template fitting on $w(\theta)$ measured on Flagship in blue, or a noise-free synthetic $w(\theta)$ computed like the theoretical model in orange. We first remove one redshift bin at a time. With the measured $w(\theta)$, redshift bin 11 seems to have a large weight in shifting h towards smaller values: when it is excluded, we recover a less biased estimate of h, Ω_{b}, and Ω_{cdm} with a shift of 0.3, 0.2, and $0.4\,\sigma$ respectively. Removing the other bins has a much smaller effect. Results are also shown when removing redshift bins with no BAO detection (bins 1, 4, and 6), low-redshift bins (1 to 8), and high-redshift bins (9 to 13). Apart from the effect seen from removing bin 11, we find that high-redshift bins tend to bias h towards lower values while Ω_{b} and Ω_{cdm} are biased towards larger values. However, high-redshift bins also provide the tightest constraints, with an increase of the uncertainty of h, Ω_{b}, and Ω_{cdm} by 23%, 30%, and 87% respectively when they are removed. Replacing α_i obtained from the measured $w(\theta)$ by the ones from a synthetic $w(\theta)$, we find that
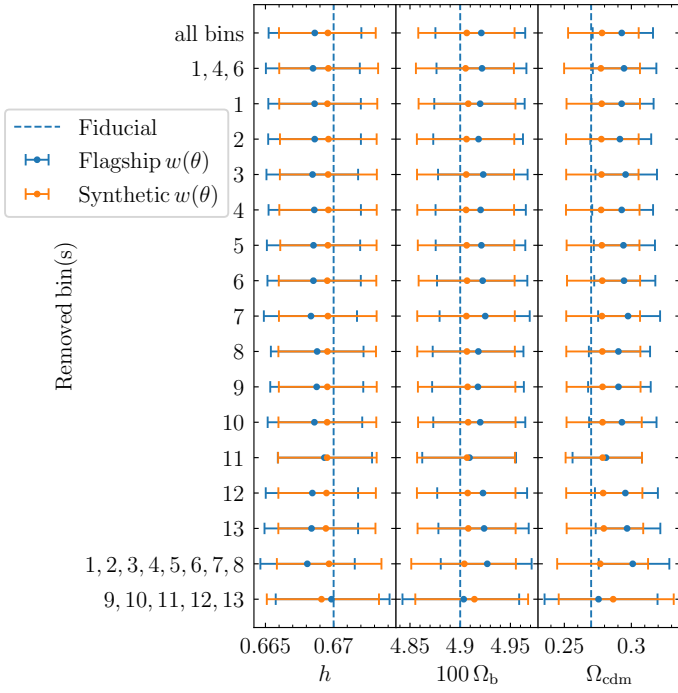
Fig. 7. Comparison of cosmological parameters obtained when one or several redshift bins are removed from the analysis. The fiducial values of the simulation are highlighted as a vertical dashed line. The baseline including all bins is shown at the top as a reference. The results in blue and orange are respectively obtained from the α_i extracted by template fitting of the $w(\theta)$ measured on Flagship and a noise-free synthetic $w(\theta)$.

shifts of h, Ω_b, and Ω_{cdm} (shown in orange in Fig. 7) with respect to their fiducial values are on average decreasing from 0.4, 0.4, and $0.9\,\sigma$ to 0.1, 0.1, and $0.3\,\sigma$. The constraining power is also robust with respect to the choice of bins when excluded one by one, with an average variation smaller than 2% for h and Ω_b, and 7% for Ω_{cdm}. With the synthetic data vector, the increase of the uncertainties when removing high redshifts is smaller with 16%, 17%, and 63% against 23%, 30%, and 87% with the measured $w(\theta)$.

5.5. Comparison of fitting templates

The polynomial correction applied in the template is defined arbitrarily and different choices can be found in the literature. It is important to check whether the polynomial includes enough orders to absorb eventual non-linearities of the galaxy bias. In this context, we explore ten different combinations of orders leading to ten templates using the same scale cuts and fiducial cosmology as for the analysis of the individual bins. The templates considered in this analysis are

- template 1: $B\,w_{\mathrm{fid}}(\alpha\theta) + A_0 + A_1\,\theta^{-1} + A_2\,\theta^{-2}$,
- template 2: $B\,w_{\mathrm{fid}}(\alpha\theta) + A_0 + A_1\theta + A_2\,\theta^{-1}$,
- template 3: $B\,w_{\mathrm{fid}}(\alpha\theta) + A_0 + A_1\theta + A_2\,\theta^{-2}$,
- template 4: $B\,w_{\mathrm{fid}}(\alpha\theta) + A_0 + A_1\theta + A_2\theta^2$,
- template 5: $B\,w_{\mathrm{fid}}(\alpha\theta) + A_0 + A_1\,\theta^{-1} + A_2\theta^2$,
- template 6: $B\,w_{\mathrm{fid}}(\alpha\theta) + A_0 + A_1\,\theta^{-1}$,
- template 7: $B\,w_{\mathrm{fid}}(\alpha\theta) + A_0 + A_1\,\theta^{-1} + A_2\,\theta^{-2} + A_3\,\theta^{-3}$,
- template 8: $B\,w_{\mathrm{fid}}(\alpha\theta) + A_0 + A_1\,\theta^{-1} + A_2\,\theta^{-2} + A_3\,\theta^{-3} + A_4\,\theta^{-4}$,
- template 9: $B\,w_{\mathrm{fid}}(\alpha\theta) + A_0 + A_1\,\theta^{-1} + A_2\,\theta^{-2} + A_3\theta$,
- template 10: $B\,w_{\mathrm{fid}}(\alpha\theta) + A_0 + A_1\,\theta^{-1} + A_2\,\theta^{-2} + A_3\theta + A_4\theta^2$.

The comparison of the resulting α for each template with respect to the fiducial template 1 is shown in Fig. 8. Constraints

from templates 2, 4, 5, and 6 are highlighted because they are consistent with each other and quite different from the reference at low redshift. These templates do not have a term in $1/\theta^2$. From this observation, it seems that this order is needed. We find that the $1\,\sigma$ uncertainty on α is systematically underestimated by 10% with templates 2, 4, 5, and 6. This result is still observed when a noise-free synthetic data vector is used instead of the measured two-point correlation function. On the contrary, we see almost no variation of the results between the other templates with additional orders $\theta^{-3}, \theta^{-4}, \theta, \theta^2$. The agreement of the various measurements of α with these templates defined as $|\alpha - \alpha_{\mathrm{ref}}|\left(\sigma^2 + \sigma_{\mathrm{ref}}^2\right)^{-1/2}$ remains within $0.15\,\sigma$. This trend is also observed when cosmological constraints are inferred, with a small but very clear shift in the posterior distributions of Ω_{cdm} for templates 2, 4, 5, and 6, as shown in Fig. 9. Given the similar constraints between the other templates, template 1 was chosen for the main analysis.

Another important aspect of the robustness of the template is to be able to handle shifts of the fiducial cosmology with respect to the true cosmology. As such, the previous comparison has been repeated in a setup where the fiducial cosmology was altered to differ from the cosmology from the Flagship simulation, using $h = 0.73$ instead of $h = 0.67$. In this case, we find that the absolute shift of α with respect to the expected value of 1 averaged over all redshift bins $\langle|1 - \alpha|\rangle$ for templates 1, 3, 7, 8, 9, 10 (we exclude templates without order θ^{-2}) is respectively 0.030, 0.033, 0.030, 0.030, 0.031, and 0.032. Table 4 presents the results of this test, showing no preference for including higher orders in the template polynomial when it comes to robustness with respect to the choice of fiducial cosmology.

5.6. Effect of the scale cuts

The large redshift range $0.2 \leq z \leq 2.5$ included in this configuration space analysis entails that θ_{BAO} varies between $1°6$ and $7°0$. In this situation, using a single scale cut for all bins or a redshift-dependent one is not obvious. We performed a first study of how α varies as a function of $\theta_{\min}$ and $\theta_{\max}$ with a fitting approach on a grid defined by $\theta_{\min} \in [0°2, \theta_{\mathrm{BAO}} - 1°0]$ and $\theta_{\max} \in [\theta_{\mathrm{BAO}} + 1°0, \theta_{\mathrm{BAO}} + 3°0]$ by steps of $0°1$. The smallest data vector considered is $\theta_{\mathrm{BAO}} \pm 1°0$ with 20 points.

The results of this study are shown in Fig. 10. The bias $\alpha - 1$ varies with $\theta_{\min}$, with a clear cut-off at $\theta = 1°0$. Increasing $\theta_{\min}$ beyond this cut-off tends to bias α, especially at low redshift, where the BAO signal is smeared by the non-linear evolution of large-scale structures. While a pronounced evolution of α with $\theta_{\max} - \theta_{\mathrm{BAO}}$ is visible at low redshift when $\theta_{\min} \geq 1°0$, no clear trend can be found when $\theta_{\min} \leq 1°0$, where the bias is the smallest.

Following these observations, we then carried out an MCMC study on a smaller grid defined as $\theta_{\min} \in [0°5, 0°7]$ with the same $0°1$ resolution and $\theta_{\max} \in [\theta_{\mathrm{BAO}} + 1°0, \theta_{\mathrm{BAO}} + 2°5]$ with steps of $0°5$. On this grid, no significant variation of α was observed with both $\theta_{\min}$ and $\theta_{\max} - \theta_{\mathrm{BAO}}$. The same observations were made when the analytical Gaussian covariance was used instead of the jackknife covariance. The final scale cut chosen was then $\theta_{\min} = 0°6$, $\theta_{\max} = \theta_{\mathrm{BAO}} + 2°5$ as it yielded the most robust results across all redshift bins. In the $\theta_{\min}, \theta_{\max}$ grid used for the MCMC, the α_i extracted in all bins are in agreement within $0.06\,\sigma$ on average and at most $0.25\,\sigma$. The effect on h, Ω_b, and Ω_{cdm} inferred from the α_i is on average $0.05\,\sigma$ and never exceeds $0.14\,\sigma$.
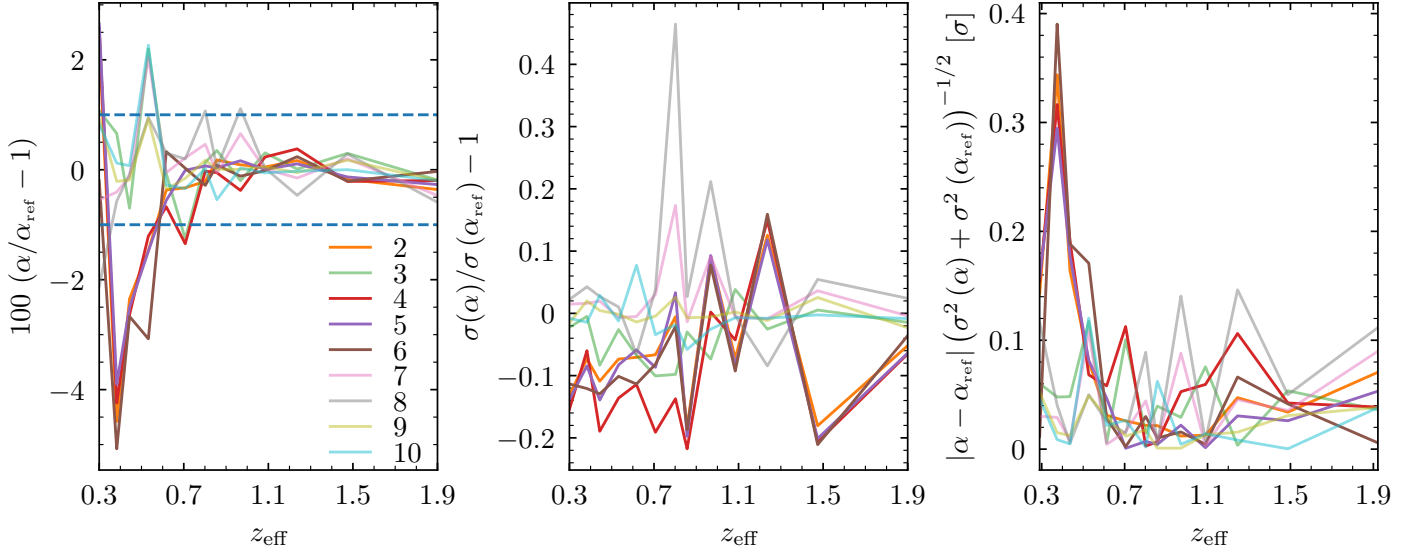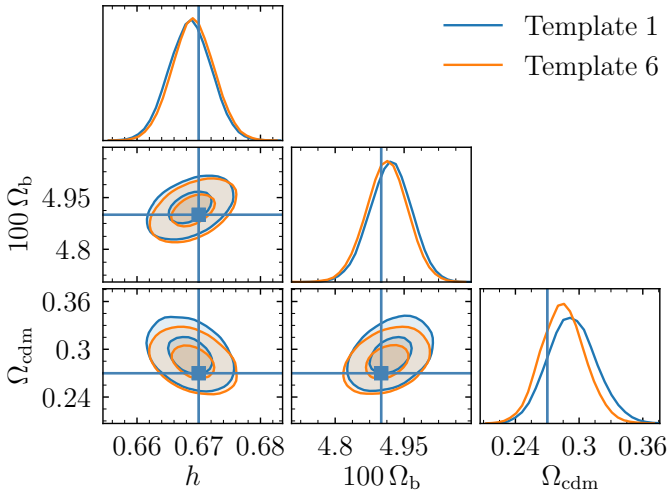
Fig. 8. Comparison of templates for BAO fitting as a function of redshift bin. The first panel represents the shift of α with respect to the reference (template 1). We highlight by transparency templates 2, 4, 5, and 6 which do not include a term in θ^{-2} to showcase the fact that they all have larger shifts at low redshift. The 1% dashed blue lines are a reference to guide the eye rather than a goal, given that the uncertainty on α is much larger in the first bins. In the second panel, we see that the highlighted templates underestimate the uncertainty while the last panel represents the agreement of the various measurements computed in sigmas as $|\alpha - \alpha_{\mathrm{ref}}| \left(\sigma^2 + \sigma_{\mathrm{ref}}^2\right)^{-1/2}$.

Table 4. Values of α obtained with the reference template 1 and templates including higher polynomial orders using a fiducial cosmology which differs from the simulation cosmology ($h = 0.73$ against $h = 0.67$). The columns $\langle|1 - \alpha|\rangle$ and $\langle\sigma_{68}\rangle$ are respectively the bias and the uncertainty of α averaged over all redshift bins. We find that template 1 has the smallest $\langle\sigma_{68}\rangle$ among templates of minimum bias $\langle|1 - \alpha|\rangle = 0.03$.

| Template	Bin 1	Bin 2	Bin 3	Bin 4	Bin 5	Bin 6	Bin 7	Bin 8	Bin 9	Bin 10	Bin 11	Bin 12	Bin 13	$\langle|1 - \alpha|\rangle$	$\langle\sigma_{68}\rangle$
1	1.013	1.046	0.969	1.011	1.012	0.996	0.949	1.069	1.047	1.032	1.049	1.011	1.010	0.030	0.068
3	1.038	1.057	0.956	1.014	1.003	0.979	0.949	1.066	1.038	1.033	1.048	1.012	1.009	0.033	0.064
7	1.010	1.042	0.970	1.027	1.010	0.996	0.952	1.068	1.056	1.032	1.047	1.013	1.007	0.030	0.070
8	0.992	1.052	0.969	1.017	1.015	1.000	0.956	1.070	1.059	1.032	1.045	1.015	1.005	0.030	0.070
9	1.034	1.052	0.970	1.016	1.005	0.994	0.949	1.067	1.049	1.032	1.048	1.012	1.009	0.031	0.067
10	1.026	1.052	0.967	1.016	1.012	0.993	0.947	1.063	1.048	1.032	1.048	1.012	1.010	0.032	0.062

Fig. 9. Comparison of templates 1 and 6 for BAO fitting at the level of cosmological parameters. Templates 3, 7, 8, 9, and 10 show contours that are similar to the ones obtained with the reference template 1. Templates 2, 4, and 5 have similarly-biased contours like in the case of template 6. The shift that can be seen most clearly on the posterior distribution of Ω_{cdm} is the effect of omitting the polynomial term in θ^{-2}.

5.7. Impact of RSD

In this section, we check whether including RSD in the theoretical model described in Sect. 2.1 affects the constraints on α. The effect of RSD over the two-point angular correlation function is illustrated in Fig. 11. The correlation function amplitude is increased at large scales and low redshift. This is the Kaiser effect, explained by the inflow of galaxies towards overdensities, which is stronger at low redshift (Kaiser 1987).

However, the actual position of the BAO scale remains unchanged and we see in Fig. 12 that this is reflected in the constraints obtained from MCMC analysis. When RSD are included, in blue in the figure, the template nuisance parameters compensate for the effect of RSD with a significant decrease of A_1, while A_0 and A_2 are slightly increased. This trend holds in all redshift bins except the last one where the amplitude of the shifts becomes negligible. The relative difference $|\Delta\alpha|/\alpha$ averaged over all redshift bins is 0.25%, the maximum being 0.5%. As for the uncertainty of α, its variations do not exceed 3.7% and are on average 1.4%. Thanks to the template-fitting approach, the analysis is robust with respect to RSD. In any case, as explained in Sect. 2.1, RSD are included in the analysis.
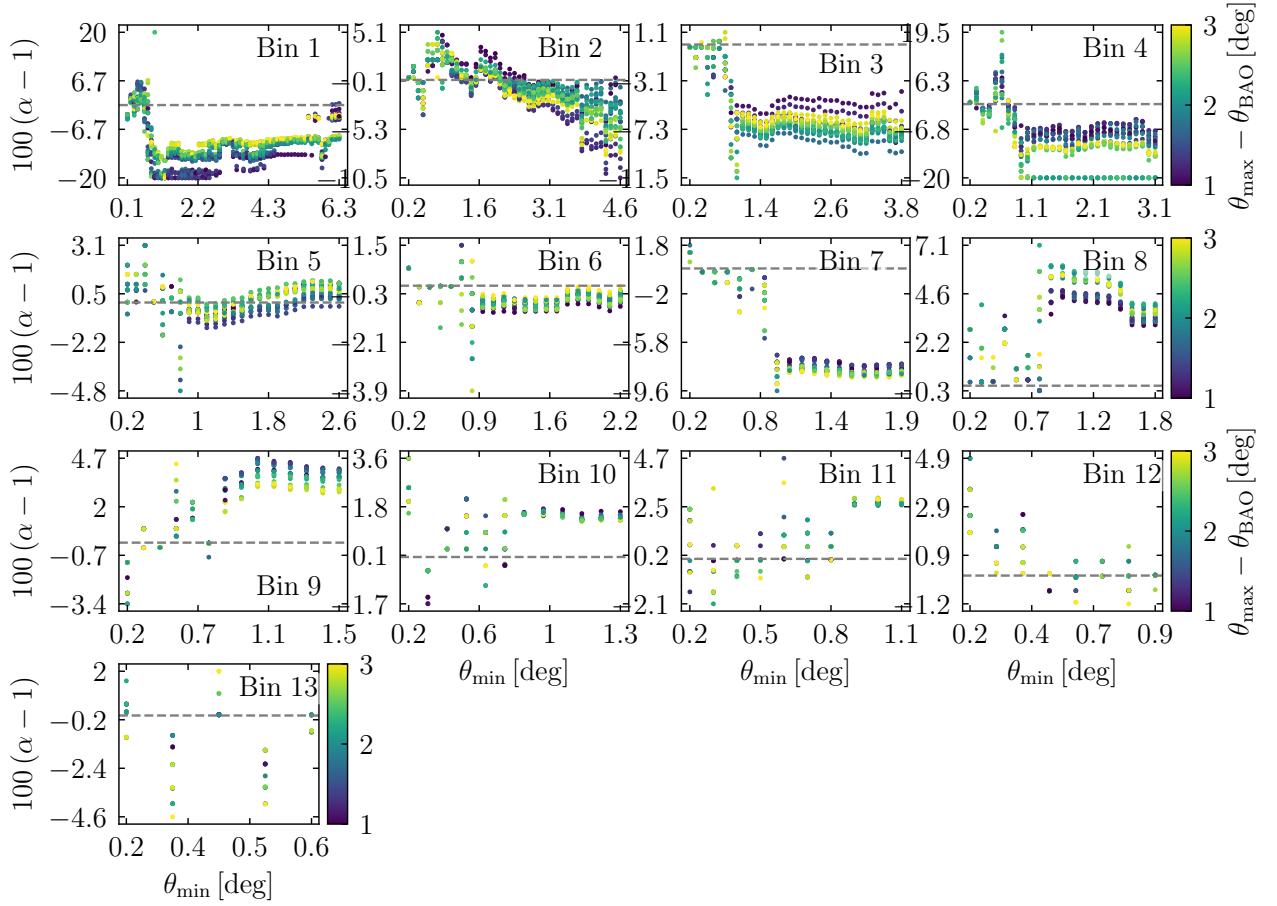
Fig. 10. Bias $100\,(\alpha - 1)$ as a function of $\theta_{\min}$ and $\theta_{\max}$ (colour) in the 13 redshift bins of the analysis. The dashed line corresponds to $\alpha - 1 = 0$. In this analysis, α is obtained by best fit rather than MCMC. In almost all redshift bins, including small scales helps in recovering an unbiased estimate of α.
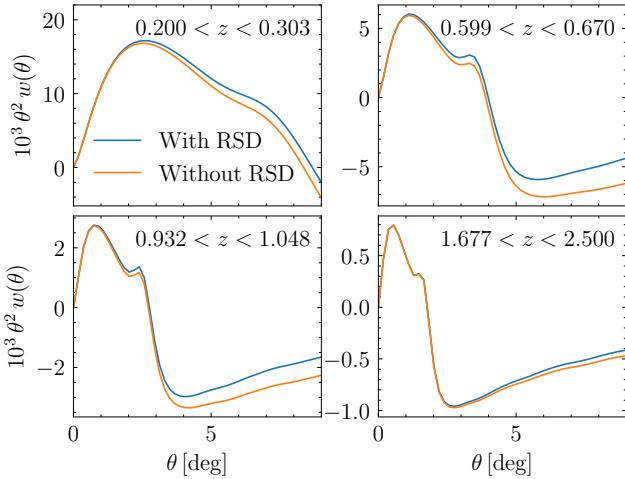
Fig. 11. Theoretical two-point correlation function computed with and without RSD using the redshift distributions of four redshift bins from the Flagship simulation shown in Fig. 1.

5.8. Effect of the redshift binning scheme

In this section, we show the effect of the choice of using equidistant redshift bins compared to the constraints obtained with equipopulated bins while keeping the same fiducial choice of template and scale cuts. This choice results in bins of width $\Delta z = 0.177$. For this analysis, the two-point correlation func-

tion and galaxy bias are measured in the same way as described in Sect. 2.2 for the equipopulated binning scheme. The rest of the analysis is carried out in an identical way. Using this binning scheme, we get equivalent constraints for redshift bins of similar z_{eff}, as reported in Table 5. Note that the equidistant binning does not entail regularly spaced z_{eff}. The effective redshifts are still computed with Eq. (21). By construction, we have more bins with high z_{eff} where the BAO signal is not smeared by the non-linear evolution of structures due to gravitation. Simultaneously, thinner redshift bins present a BAO signal which is less diluted by intra-bin variations of the BAO scale. However, the decrease in number density entails that the error bars of the two-point correlation function are larger at high redshift. In our case, this compromise yields more bins with high detection levels and tight constraints on α. We also find several bins with low values of α, two of them being more than $1\,\sigma$ away from $\alpha = 1$, at $z_{\mathrm{eff}} = 1.993$ and 2.174.

Propagating these results to the cosmological parameters, we find $h = 0.670^{+0.003}_{-0.003}$, $100\,\Omega_{\mathrm{b}} = 4.895^{+0.044}_{-0.045}$, and $\Omega_{\mathrm{cdm}} = 0.266^{+0.017}_{-0.016}$, which represents shifts of $+0.1\%$, -0.5%, and $+9.2\%$ respectively, and a 36.4% improvement in the constraining power for Ω_{cdm} with respect to the equipopulated binning results. The variations in the parameter values are driven by the low α value and tight constraints of bin 11 in the equidistant binning. Bin 12 has an even lower value $\alpha = 0.937$ and participates to these variations but in a weaker way due to its uncertainty, larger than in bin 11 by a factor 2.1. Given these results, it seems that the equidistant scheme may be more suitable for the BAO
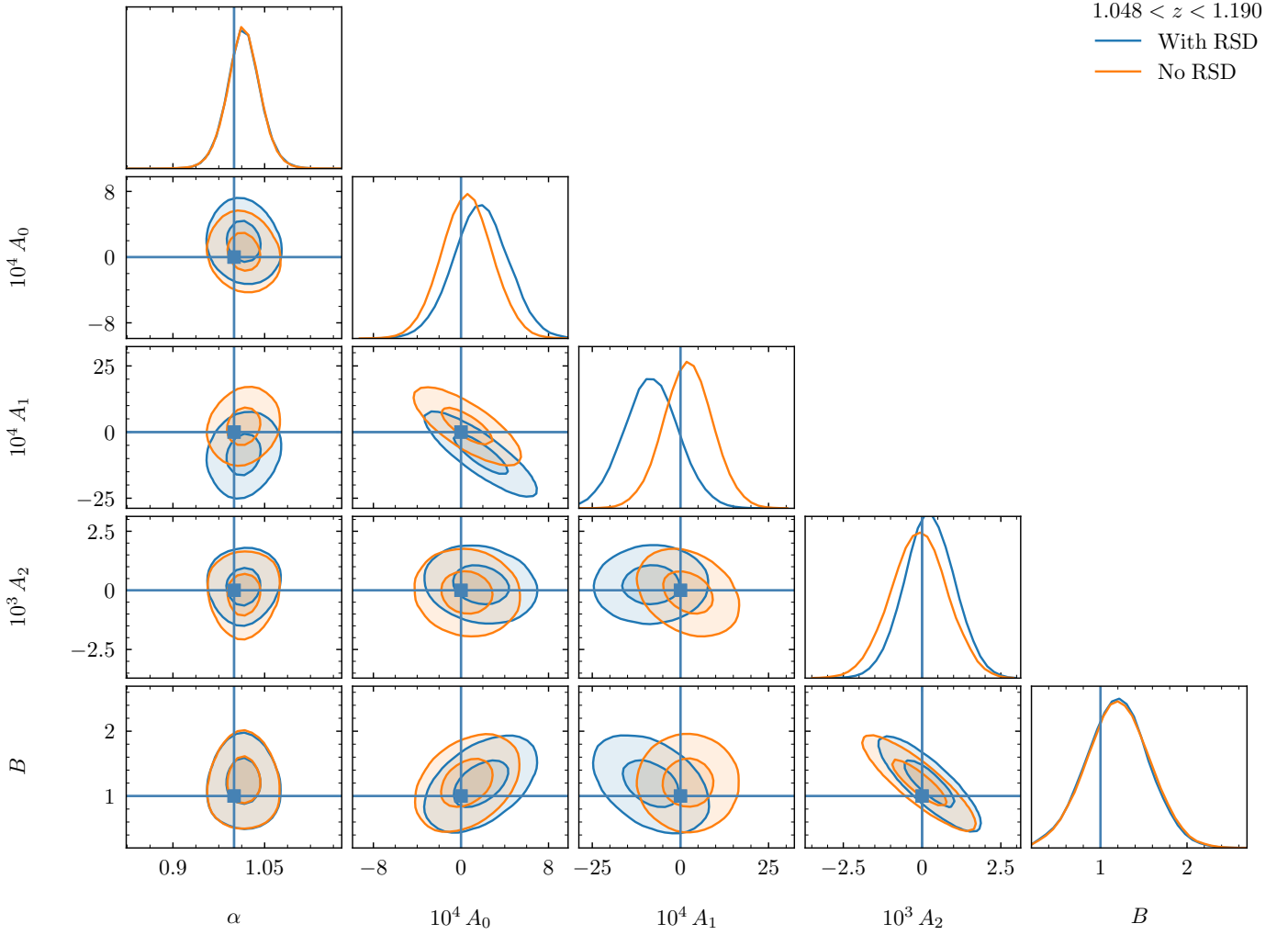
Fig. 12. Comparison of the constraints on α with and without RSD in the theoretical model for the redshift bin $1.048 < \mathrm{z} < 1.190$. The posterior distribution of α is visually identical, the effect of RSD is completely absorbed by nuisance parameters.

analysis than the equipopulated scheme initially chosen to match the choice that maximizes the dark energy figure of merit of the 3×2-point analysis for *Euclid*. In future *Euclid* BAO photometric analyses, an optimization of the photometric sample selection will by necessary.

6. Conclusions

In this work, we have estimated our ability to constrain cosmological parameters with the photometric sample of *Euclid* through a BAO analysis of the Flagship mock galaxy catalogue, whose area is intermediate to the expected observed survey area at Data Release 1 and 2. We have measured the two-point correlation function in 13 redshift bins. We have extracted constraints on the BAO signal through the α parameter in each redshift bin but also using all bins jointly. The significance of the BAO detection has been quantified to reach $\Delta_{\mathrm{det}} = 10.3\,\sigma$ with the joint analysis, a three-fold improvement with respect to the latest results in photometric surveys (DES Y6), with similar or better constraints in all redshift bins, covering also a large range of redshifts $0.2 \leq z \leq 2.5$. This result shows how powerful photometric galaxy clustering can be with *Euclid*. From these BAO constraints and considering *Planck* priors, we have derived constraints on different cosmological parameters: $h = 0.669 \pm 0.003$,

$100\,\Omega_{\mathrm{b}} = 4.921^{+0.044}_{-0.046}$, and $\Omega_{\mathrm{cdm}} = 0.293^{+0.023}_{-0.022}$ in a flat ΛCDM cosmology.

We have also studied different analysis choices, showing that scale cuts can have a non-negligible effect over the value of the α parameter. Indeed, if $\theta_{\mathrm{min}} > 1°$, then we observe a bias, even for low-redshift bins where the BAO peak is at large scales. On the contrary, while omitting the order θ^{-2} in the template biases the resulting cosmological constraints, there is no need to include higher orders in the template functional form used to fit the BAO feature. The template is robust to the choice of fiducial cosmology, with variations $|\Delta\alpha|/\alpha$ not exceeding 0.0031 when averaged over all redshifts, well below the uncertainties of α given in Table 2. The template is efficient when it comes to absorbing effects that affect the amplitude of the two-point angular correlation function like RSD: including or removing them from the model, the constraints over α remain unchanged at all redshifts. An important point which has been seen in both joint and individual redshift bin analyses is the robustness with respect to the redshift bins included in the analysis. We have also checked that there is no significant bias when a synthetic data vector is used. However, when we consider the data vector measured on the Flagship simulation, we have observed a shift of the α parameter and an increase of its uncertainty when redshift bin 11 is excluded. This effect is seen in both the joint analysis and the

Table 5. Values of α extracted from MCMC in each equidistant redshift bin. The detection level is defined in Eq. (22). As there are more redshift bins at higher redshifts, the detection of the BAO signal is stronger than with equipopulated bins, increasing the constraining power over cosmological parameters.

Bin	z_{eff}	α	Δ_{det} (σ)
1	0.311	$1.076^{+0.090}_{-0.145}$	no detection
2	0.442	$0.974^{+0.145}_{-0.114}$	1.0
3	0.63	$0.971^{+0.086}_{-0.089}$	no detection
4	0.806	$0.946^{+0.076}_{-0.063}$	1.2
5	0.961	$1.033^{+0.056}_{-0.060}$	1.3
6	1.126	$1.007^{+0.052}_{-0.049}$	2.0
7	1.286	$1.022^{+0.022}_{-0.022}$	4.1
8	1.474	$1.005^{+0.035}_{-0.032}$	2.5
9	1.641	$0.955^{+0.050}_{-0.042}$	2.2
10	1.82	$0.996^{+0.028}_{-0.028}$	3.4
11	1.993	$0.962^{+0.028}_{-0.025}$	3.3
12	2.174	$0.937^{+0.057}_{-0.045}$	2.0
13	2.365	$1.001^{+0.018}_{-0.018}$	4.6

cosmological parameters inferred from α_i, $i \in [1, 13]$. This is explained by the fact that this bin has the largest BAO detection significance. This detailed study of the effect of each redshift bin will be mandatory in future works, given that the strength of the BAO signal and its effect over cosmological constraints change with redshift.

Results from Sect. 5.8 suggest that there is margin for improvement in the constraints obtained from a BAO analysis by optimising the redshift binning scheme. A galaxy sample selection taking into account both redshift and colour could be another possible point of improvement for these results. However, it is very promising to see that with a simulated area of 37% of what is expected at Data Release 3 of *Euclid*, the constraints on α are already improved by a factor three with respect to the current best constraints from a single photometric survey.

References

Abbott, T. M. C., Abdalla, F. B., Allam, S., et al. 2018, ApJS, 239, 18
Abbott, T. M. C., Adamow, M., Aguena, M., et al. 2024, Phys. Rev. D, 110, 063515
Ade, P. A. R., Aghanim, N., Arnaud, M., et al. 2016, A&A, 594, A13
Ade, P. A. R., Aghanim, N., Arnaud, M., et al. 2014, A&A, 566, A54
Alonso, D., Bull, P., Ferreira, P. G., Maartens, R., & Santos, M. G. 2015, ApJ, 814, 145
Behroozi, P. S., Wechsler, R. H., & Wu, H.-Y. 2013, ApJ, 762, 109
Blanton, M. R., Hogg, D. W., Bahcall, N. A., et al. 2003, ApJ, 592, 819
Blanton, M. R., Lupton, R. H., Schlegel, D. J., et al. 2005a, ApJ, 631, 208
Blanton, M. R., Schlegel, D. J., Strauss, M. A., et al. 2005b, AJ, 129, 2562
Blas, D., Lesgourgues, J., & Tram, T. 2011, JCAP, 07, 034
Carretero, J., Castander, F. J., Gaztañaga, E., Crocce, M., & Fosalba, P. 2015, MNRAS, 447, 646
Carretero, J., Tallada, P., Casals, J., et al. 2017, in Proceedings of the European Physical Society Conference on High Energy Physics. 5-12 July, 488
Challinor, A. & Lewis, A. 2011, Phys. Rev. D, 84, 043516
Chisari, N. E., Alonso, D., Krause, E., et al. 2019, ApJS, 242, 2
Cole, S., Percival, W. J., Peacock, J. A., et al. 2005, MNRAS, 362, 505
Crocce, M., Cabré, A., & Gaztañaga, E. 2011, MNRAS, 414, 329
Dahlen, T., Mobasher, B., Somerville, R. S., et al. 2005, ApJ, 631, 126
Dembinski, H., Ongmongkolkul, P., Deil, C., et al. 2020, Zenodo, 10.5281/zenodo.3949207
DESI Collaboration: Adame, A., Aguilar, J., Ahlen, S., et al. 2024, arXiv e-prints, arXiv:2404.03000
Eisenstein, D. J. & Hu, W. 1998, ApJ, 496, 605
Eisenstein, D. J., Zehavi, I., Hogg, D. W., et al. 2005, ApJ, 633, 560
Euclid Collaboration : Sciotti, D., Gouyou Beauchamps, S., Cardone, V. F., et al. 2024, A&A, 691, A318
Euclid Collaboration: Blanchard, A., Camera, S., Carbone, C., et al. 2020, A&A, 642, A191
Euclid Collaboration: Castander, F. J., Fosalba, P., Stadel, J., et al. 2024, A&A, accepted, arXiv:2405.13495
Euclid Collaboration: Cropper, M., Al-Bahlawan, A., Amiaux, J., et al. 2024, A&A, accepted, arXiv:2405.13492
Euclid Collaboration: Jahnke, K., Gillard, W., Schirmer, M., et al. 2024, A&A, accepted, arXiv:2405.13493
Euclid Collaboration: Mellier, Y., Abdurro'uf, Acevedo Barroso, J. A., et al. 2024, A&A, accepted, arXiv:2405.13491
Fang, X., Eifler, T., & Krause, E. 2020b, MNRAS, 497, 2699
Fang, X., Krause, E., Eifler, T., & MacCrann, N. 2020a, JCAP, 05, 010
Foreman-Mackey, D., Hogg, D. W., Lang, D., & Goodman, J. 2013, PASP, 125, 306
Gelman, A. & Rubin, D. B. 1992, Statistical Science, 7, 457
Górski, K. M., Hivon, E., Banday, A. J., et al. 2005, ApJ, 622, 759
Gouyou Beauchamps, S., Lacasa, F., Tutusaus, I., et al. 2022, A&A, 659, A128
Hartlap, J., Simon, P., & Schneider, P. 2007, A&A, 464, 399
Hu, W. & Sugiyama, N. 1996, ApJ, 471, 542
Ivezić, Ž., Kahn, S. M., Tyson, J. A., et al. 2019, ApJ, 873, 111
James, F. & Roos, M. 1975, Comput. Phys. Commun., 10, 343
Jarvis, M., Bernstein, G., & Jain, B. 2004, MNRAS, 352, 338
Kaiser, N. 1987, MNRAS, 227, 1
Kaiser, N. 1992, ApJ, 388, 272
Krause, E. & Eifler, T. 2017, MNRAS, 470, 2100
Lacasa, F. & Grain, J. 2019, A&A, 624, A61
Landy, S. D. & Szalay, A. S. 1993, ApJ, 412, 64
Lepori, F., Tutusaus, I., Viglione, C., et al. 2022, A&A, 662, A93
Lewis, A., Challinor, A., & Lasenby, A. 2000, ApJ, 538, 473
Mather, J. C., Fixsen, D. J., Shafer, R. A., Mosier, C., & Wilkinson, D. T. 1999, ApJ, 512, 511
Mead, A. J., Brieden, S., Tröster, T., & Heymans, C. 2021, MNRAS, 502, 1401
Percival, W. J., Baugh, C. M., Bland-Hawthorn, J., et al. 2001, MNRAS, 327, 1297
Potter, D., Stadel, J., & Teyssier, R. 2017, CompAC, 4, 2
Tallada, P., Carretero, J., Casals, J., et al. 2020, Astronomy and Computing, 32, 100391
Tanaka, M., Coupon, J., Hsieh, B.-C., et al. 2018, PASJ, 70, S9
Troxel, M. A., Krause, E., Chang, C., et al. 2018, MNRAS, 479, 4998
Tutusaus, I., Martinelli, M., Cardone, V. F., et al. 2020, A&A, 643, A70
Zehavi, I., Zheng, Z., Weinberg, D. H., et al. 2011, ApJ, 736, 59
Zonca, A., Singer, L., Lenz, D., et al. 2019, Journal of Open Source Software, 4, 1298

1 Aix-Marseille Université, CNRS/IN2P3, CPPM, Marseille, France
2 Institut de Recherche en Astrophysique et Planétologie (IRAP), Université de Toulouse, CNRS, UPS, CNES, 14 Av. Edouard Belin, 31400 Toulouse, France
3 Dipartimento di Fisica, Università degli Studi di Torino, Via P. Giuria 1, 10125 Torino, Italy
4 INFN-Sezione di Torino, Via P. Giuria 1, 10125 Torino, Italy
5 INAF-Osservatorio Astrofisico di Torino, Via Osservatorio 20, 10025 Pino Torinese (TO), Italy
6 Department of Physics and Astronomy, University College London, Gower Street, London WC1E 6BT, UK
7 Institute of Space Sciences (ICE, CSIC), Campus UAB, Carrer de Can Magrans, s/n, 08193 Barcelona, Spain
8 Institut d'Estudis Espacials de Catalunya (IEEC), Edifici RDIT, Campus UPC, 08860 Castelldefels, Barcelona, Spain
9 Université Paris-Saclay, CNRS, Institut d'astrophysique spatiale, 91405, Orsay, France
10 School of Mathematics and Physics, University of Surrey, Guildford, Surrey, GU2 7XH, UK
11 Institut für Theoretische Physik, University of Heidelberg, Philosophenweg 16, 69120 Heidelberg, Germany
12 INAF-Osservatorio Astronomico di Brera, Via Brera 28, 20122 Milano, Italy
13 INAF-Osservatorio di Astrofisica e Scienza dello Spazio di Bologna, Via Piero Gobetti 93/3, 40129 Bologna, Italy
14 IFPU, Institute for Fundamental Physics of the Universe, via Beirut 2, 34151 Trieste, Italy
15 INAF-Osservatorio Astronomico di Trieste, Via G. B. Tiepolo 11, 34143 Trieste, Italy
16 INFN, Sezione di Trieste, Via Valerio 2, 34127 Trieste TS, Italy
17 SISSA, International School for Advanced Studies, Via Bonomea 265, 34136 Trieste TS, Italy
18 Dipartimento di Fisica e Astronomia, Università di Bologna, Via Gobetti 93/2, 40129 Bologna, Italy
19 INFN-Sezione di Bologna, Viale Berti Pichat 6/2, 40127 Bologna, Italy
20 Dipartimento di Fisica, Università di Genova, Via Dodecaneso 33, 16146, Genova, Italy
21 INFN-Sezione di Genova, Via Dodecaneso 33, 16146, Genova, Italy
22 Department of Physics "E. Pancini", University Federico II, Via Cinthia 6, 80126, Napoli, Italy
23 INAF-Osservatorio Astronomico di Capodimonte, Via Moiariello 16, 80131 Napoli, Italy
24 INFN section of Naples, Via Cinthia 6, 80126, Napoli, Italy
25 Instituto de Astrofísica e Ciências do Espaço, Universidade do Porto, CAUP, Rua das Estrelas, PT4150-762 Porto, Portugal
26 Faculdade de Ciências da Universidade do Porto, Rua do Campo de Alegre, 4150-007 Porto, Portugal
27 Aix-Marseille Université, CNRS, CNES, LAM, Marseille, France
28 European Space Agency/ESTEC, Keplerlaan 1, 2201 AZ Noordwijk, The Netherlands
29 Institute Lorentz, Leiden University, Niels Bohrweg 2, 2333 CA Leiden, The Netherlands
30 INAF-IASF Milano, Via Alfonso Corti 12, 20133 Milano, Italy
31 INAF-Osservatorio Astronomico di Roma, Via Frascati 33, 00078 Monteporzio Catone, Italy
32 INFN-Sezione di Roma, Piazzale Aldo Moro, 2 - c/o Dipartimento di Fisica, Edificio G. Marconi, 00185 Roma, Italy
33 Centro de Investigaciones Energéticas, Medioambientales y Tecnológicas (CIEMAT), Avenida Complutense 40, 28040 Madrid, Spain
34 Port d'Informació Científica, Campus UAB, C. Albareda s/n, 08193 Bellaterra (Barcelona), Spain
35 Institute for Theoretical Particle Physics and Cosmology (TTK), RWTH Aachen University, 52056 Aachen, Germany
36 Institute of Cosmology and Gravitation, University of Portsmouth, Portsmouth PO1 3FX, UK
37 Institute for Astronomy, University of Hawaii, 2680 Woodlawn Drive, Honolulu, HI 96822, USA
38 Dipartimento di Fisica e Astronomia "Augusto Righi" - Alma Mater Studiorum Università di Bologna, Viale Berti Pichat 6/2, 40127 Bologna, Italy
39 Instituto de Astrofísica de Canarias, Vía Láctea, 38205 La Laguna, Tenerife, Spain
40 Institute for Astronomy, University of Edinburgh, Royal Observatory, Blackford Hill, Edinburgh EH9 3HJ, UK
41 Jodrell Bank Centre for Astrophysics, Department of Physics and Astronomy, University of Manchester, Oxford Road, Manchester M13 9PL, UK
42 European Space Agency/ESRIN, Largo Galileo Galilei 1, 00044 Frascati, Roma, Italy
43 ESAC/ESA, Camino Bajo del Castillo, s/n., Urb. Villafranca del Castillo, 28692 Villanueva de la Cañada, Madrid, Spain
44 Université Claude Bernard Lyon 1, CNRS/IN2P3, IP2I Lyon, UMR 5822, Villeurbanne, F-69100, France
45 Institut de Ciències del Cosmos (ICCUB), Universitat de Barcelona (IEEC-UB), Martí i Franquès 1, 08028 Barcelona, Spain
46 Institució Catalana de Recerca i Estudis Avançats (ICREA), Passeig de Lluís Companys 23, 08010 Barcelona, Spain
47 UCB Lyon 1, CNRS/IN2P3, IUF, IP2I Lyon, 4 rue Enrico Fermi, 69622 Villeurbanne, France
48 Mullard Space Science Laboratory, University College London, Holmbury St Mary, Dorking, Surrey RH5 6NT, UK
49 Departamento de Física, Faculdade de Ciências, Universidade de Lisboa, Edifício C8, Campo Grande, PT1749-016 Lisboa, Portugal
50 Instituto de Astrofísica e Ciências do Espaço, Faculdade de Ciências, Universidade de Lisboa, Campo Grande, 1749-016 Lisboa, Portugal
51 Department of Astronomy, University of Geneva, ch. d'Ecogia 16, 1290 Versoix, Switzerland
52 INAF-Istituto di Astrofisica e Planetologia Spaziali, via del Fosso del Cavaliere, 100, 00100 Roma, Italy
53 INFN-Padova, Via Marzolo 8, 35131 Padova, Italy
54 Université Paris-Saclay, Université Paris Cité, CEA, CNRS, AIM, 91191, Gif-sur-Yvette, France
55 Space Science Data Center, Italian Space Agency, via del Politecnico snc, 00133 Roma, Italy
56 INFN-Bologna, Via Irnerio 46, 40126 Bologna, Italy
57 School of Physics, HH Wills Physics Laboratory, University of Bristol, Tyndall Avenue, Bristol, BS8 1TL, UK
58 Max Planck Institute for Extraterrestrial Physics, Giessenbachstr. 1, 85748 Garching, Germany
59 INAF-Osservatorio Astronomico di Padova, Via dell'Osservatorio 5, 35122 Padova, Italy
60 Universitäts-Sternwarte München, Fakultät für Physik, Ludwig-Maximilians-Universität München, Scheinerstrasse 1, 81679 München, Germany
61 Institute of Theoretical Astrophysics, University of Oslo, P.O. Box 1029 Blindern, 0315 Oslo, Norway
62 Jet Propulsion Laboratory, California Institute of Technology, 4800 Oak Grove Drive, Pasadena, CA, 91109, USA
63 Felix Hormuth Engineering, Goethestr. 17, 69181 Leimen, Germany
64 Technical University of Denmark, Elektrovej 327, 2800 Kgs. Lyngby, Denmark
65 Cosmic Dawn Center (DAWN), Denmark
66 Institut d'Astrophysique de Paris, UMR 7095, CNRS, and Sorbonne Université, 98 bis boulevard Arago, 75014 Paris, France
67 Max-Planck-Institut für Astronomie, Königstuhl 17, 69117 Heidelberg, Germany
68 NASA Goddard Space Flight Center, Greenbelt, MD 20771, USA
69 Department of Physics and Helsinki Institute of Physics, Gustaf Hällströmin katu 2, 00014 University of Helsinki, Finland
70 Université de Genève, Département de Physique Théorique and Centre for Astroparticle Physics, 24 quai Ernest-Ansermet, CH-1211 Genève 4, Switzerland

71 Department of Physics, P.O. Box 64, 00014 University of Helsinki, Finland

72 Helsinki Institute of Physics, Gustaf Hällströmin katu 2, University of Helsinki, Helsinki, Finland

73 Laboratoire Univers et Théorie, Observatoire de Paris, Université PSL, Université Paris Cité, CNRS, 92190 Meudon, France

74 SKA Observatory, Jodrell Bank, Lower Withington, Macclesfield, Cheshire SK11 9FT, UK

75 Centre de Calcul de l'IN2P3/CNRS, 21 avenue Pierre de Coubertin 69627 Villeurbanne Cedex, France

76 Dipartimento di Fisica "Aldo Pontremoli", Università degli Studi di Milano, Via Celoria 16, 20133 Milano, Italy

77 INFN-Sezione di Milano, Via Celoria 16, 20133 Milano, Italy

78 University of Applied Sciences and Arts of Northwestern Switzerland, School of Engineering, 5210 Windisch, Switzerland

79 Universität Bonn, Argelander-Institut für Astronomie, Auf dem Hügel 71, 53121 Bonn, Germany

80 Dipartimento di Fisica e Astronomia "Augusto Righi" - Alma Mater Studiorum Università di Bologna, via Piero Gobetti 93/2, 40129 Bologna, Italy

81 Department of Physics, Institute for Computational Cosmology, Durham University, South Road, Durham, DH1 3LE, UK

82 Université Côte d'Azur, Observatoire de la Côte d'Azur, CNRS, Laboratoire Lagrange, Bd de l'Observatoire, CS 34229, 06304 Nice cedex 4, France

83 Université Paris Cité, CNRS, Astroparticule et Cosmologie, 75013 Paris, France

84 CNRS-UCB International Research Laboratory, Centre Pierre Binetruy, IRL2007, CPB-IN2P3, Berkeley, USA

85 Institut d'Astrophysique de Paris, 98bis Boulevard Arago, 75014, Paris, France

86 Institute of Physics, Laboratory of Astrophysics, Ecole Polytechnique Fédérale de Lausanne (EPFL), Observatoire de Sauverny, 1290 Versoix, Switzerland

87 Aurora Technology for European Space Agency (ESA), Camino bajo del Castillo, s/n, Urbanizacion Villafranca del Castillo, Villanueva de la Cañada, 28692 Madrid, Spain

88 Institut de Física d'Altes Energies (IFAE), The Barcelona Institute of Science and Technology, Campus UAB, 08193 Bellaterra (Barcelona), Spain

89 DARK, Niels Bohr Institute, University of Copenhagen, Jagtvej 155, 2200 Copenhagen, Denmark

90 Waterloo Centre for Astrophysics, University of Waterloo, Waterloo, Ontario N2L 3G1, Canada

91 Department of Physics and Astronomy, University of Waterloo, Waterloo, Ontario N2L 3G1, Canada

92 Perimeter Institute for Theoretical Physics, Waterloo, Ontario N2L 2Y5, Canada

93 Centre National d'Etudes Spatiales – Centre spatial de Toulouse, 18 avenue Edouard Belin, 31401 Toulouse Cedex 9, France

94 Institute of Space Science, Str. Atomistilor, nr. 409 Măgurele, Ilfov, 077125, Romania

95 Consejo Superior de Investigaciones Científicas, Calle Serrano 117, 28006 Madrid, Spain

96 Universidad de La Laguna, Departamento de Astrofísica, 38206 La Laguna, Tenerife, Spain

97 Université St Joseph; Faculty of Sciences, Beirut, Lebanon

98 Departamento de Física, FCFM, Universidad de Chile, Blanco Encalada 2008, Santiago, Chile

99 Universität Innsbruck, Institut für Astro- und Teilchenphysik, Technikerstr. 25/8, 6020 Innsbruck, Austria

100 Satlantis, University Science Park, Sede Bld 48940, Leioa-Bilbao, Spain

101 Dipartimento di Fisica e Astronomia "G. Galilei", Università di Padova, Via Marzolo 8, 35131 Padova, Italy

102 Department of Physics, Royal Holloway, University of London, TW20 0EX, UK

103 Instituto de Astrofísica e Ciências do Espaço, Faculdade de Ciências, Universidade de Lisboa, Tapada da Ajuda, 1349-018 Lisboa, Portugal

104 Cosmic Dawn Center (DAWN)

105 Niels Bohr Institute, University of Copenhagen, Jagtvej 128, 2200 Copenhagen, Denmark

106 Universidad Politécnica de Cartagena, Departamento de Electrónica y Tecnología de Computadoras, Plaza del Hospital 1, 30202 Cartagena, Spain

107 Kapteyn Astronomical Institute, University of Groningen, PO Box 800, 9700 AV Groningen, The Netherlands

108 Infrared Processing and Analysis Center, California Institute of Technology, Pasadena, CA 91125, USA

109 INAF, Istituto di Radioastronomia, Via Piero Gobetti 101, 40129 Bologna, Italy

110 Astronomical Observatory of the Autonomous Region of the Aosta Valley (OAVdA), Loc. Lignan 39, I-11020, Nus (Aosta Valley), Italy

111 Department of Physics, Oxford University, Keble Road, Oxford OX1 3RH, UK

112 ICL, Junia, Université Catholique de Lille, LITL, 59000 Lille, France

113 ICSC - Centro Nazionale di Ricerca in High Performance Computing, Big Data e Quantum Computing, Via Magnanelli 2, Bologna, Italy

114 Instituto de Física Teórica UAM-CSIC, Campus de Cantoblanco, 28049 Madrid, Spain

115 CERCA/ISO, Department of Physics, Case Western Reserve University, 10900 Euclid Avenue, Cleveland, OH 44106, USA

116 Technical University of Munich, TUM School of Natural Sciences, Physics Department, James-Franck-Str. 1, 85748 Garching, Germany

117 Max-Planck-Institut für Astrophysik, Karl-Schwarzschild-Str. 1, 85748 Garching, Germany

118 Departamento de Física Fundamental. Universidad de Salamanca. Plaza de la Merced s/n. 37008 Salamanca, Spain

119 Dipartimento di Fisica e Scienze della Terra, Università degli Studi di Ferrara, Via Giuseppe Saragat 1, 44122 Ferrara, Italy

120 Istituto Nazionale di Fisica Nucleare, Sezione di Ferrara, Via Giuseppe Saragat 1, 44122 Ferrara, Italy

121 Université de Strasbourg, CNRS, Observatoire astronomique de Strasbourg, UMR 7550, 67000 Strasbourg, France

122 Center for Data-Driven Discovery, Kavli IPMU (WPI), UTIAS, The University of Tokyo, Kashiwa, Chiba 277-8583, Japan

123 Ludwig-Maximilians-University, Schellingstrasse 4, 80799 Munich, Germany

124 Max-Planck-Institut für Physik, Boltzmannstr. 8, 85748 Garching, Germany

125 Dipartimento di Fisica - Sezione di Astronomia, Università di Trieste, Via Tiepolo 11, 34131 Trieste, Italy

126 California Institute of Technology, 1200 E California Blvd, Pasadena, CA 91125, USA

127 Department of Physics & Astronomy, University of California Irvine, Irvine CA 92697, USA

128 Department of Mathematics and Physics E. De Giorgi, University of Salento, Via per Arnesano, CP-I93, 73100, Lecce, Italy

129 INFN, Sezione di Lecce, Via per Arnesano, CP-193, 73100, Lecce, Italy

130 INAF-Sezione di Lecce, c/o Dipartimento Matematica e Fisica, Via per Arnesano, 73100, Lecce, Italy

131 Departamento Física Aplicada, Universidad Politécnica de Cartagena, Campus Muralla del Mar, 30202 Cartagena, Murcia, Spain

132 Instituto de Física de Cantabria, Edificio Juan Jordá, Avenida de los Castros, 39005 Santander, Spain

133 Department of Computer Science, Aalto University, PO Box 15400, Espoo, FI-00 076, Finland

134 Instituto de Astrofísica de Canarias, c/ Via Lactea s/n, La Laguna 38200, Spain. Departamento de Astrofísica de la Universidad de La Laguna, Avda. Francisco Sanchez, La Laguna, 38200, Spain

135 Caltech/IPAC, 1200 E. California Blvd., Pasadena, CA 91125, USA

[136] Ruhr University Bochum, Faculty of Physics and Astronomy, Astronomical Institute (AIRUB), German Centre for Cosmological Lensing (GCCL), 44780 Bochum, Germany

[137] Department of Physics and Astronomy, Vesilinnantie 5, 20014 University of Turku, Finland

[138] Serco for European Space Agency (ESA), Camino bajo del Castillo, s/n, Urbanizacion Villafranca del Castillo, Villanueva de la Cañada, 28692 Madrid, Spain

[139] ARC Centre of Excellence for Dark Matter Particle Physics, Melbourne, Australia

[140] Centre for Astrophysics & Supercomputing, Swinburne University of Technology, Hawthorn, Victoria 3122, Australia

[141] Department of Physics and Astronomy, University of the Western Cape, Bellville, Cape Town, 7535, South Africa

[142] Department of Physics, Centre for Extragalactic Astronomy, Durham University, South Road, Durham, DH1 3LE, UK

[143] IRFU, CEA, Université Paris-Saclay 91191 Gif-sur-Yvette Cedex, France

[144] Oskar Klein Centre for Cosmoparticle Physics, Department of Physics, Stockholm University, Stockholm, SE-106 91, Sweden

[145] Astrophysics Group, Blackett Laboratory, Imperial College London, London SW7 2AZ, UK

[146] INAF-Osservatorio Astrofisico di Arcetri, Largo E. Fermi 5, 50125, Firenze, Italy

[147] Dipartimento di Fisica, Sapienza Università di Roma, Piazzale Aldo Moro 2, 00185 Roma, Italy

[148] Centro de Astrofísica da Universidade do Porto, Rua das Estrelas, 4150-762 Porto, Portugal

[149] HE Space for European Space Agency (ESA), Camino bajo del Castillo, s/n, Urbanizacion Villafranca del Castillo, Villanueva de la Cañada, 28692 Madrid, Spain

[150] Department of Astrophysical Sciences, Peyton Hall, Princeton University, Princeton, NJ 08544, USA

[151] Department of Astrophysics, University of Zurich, Winterthurerstrasse 190, 8057 Zurich, Switzerland

[152] INAF-Osservatorio Astronomico di Brera, Via Brera 28, 20122 Milano, Italy, and INFN-Sezione di Genova, Via Dodecaneso 33, 16146, Genova, Italy

[153] Theoretical astrophysics, Department of Physics and Astronomy, Uppsala University, Box 515, 751 20 Uppsala, Sweden

[154] Mathematical Institute, University of Leiden, Einsteinweg 55, 2333 CA Leiden, The Netherlands

[155] Leiden Observatory, Leiden University, Einsteinweg 55, 2333 CC Leiden, The Netherlands

[156] Institute of Astronomy, University of Cambridge, Madingley Road, Cambridge CB3 0HA, UK

[157] Space physics and astronomy research unit, University of Oulu, Pentti Kaiteran katu 1, FI-90014 Oulu, Finland

[158] Institut de Physique Théorique, CEA, CNRS, Université Paris-Saclay 91191 Gif-sur-Yvette Cedex, France

[159] Center for Computational Astrophysics, Flatiron Institute, 162 5th Avenue, 10010, New York, NY, USA

Appendix A: Computation of $r_{\mathrm{s,\,drag}}$

In our analysis, we compute $r_{\mathrm{s,\,drag}}$ following the fast approximations described by Eqs. (2) to (6) in Eisenstein & Hu (1998). In these equations, we updated the CMB temperature to its value $T_{\mathrm{CMB}} = 2.725\,\mathrm{K}$ reported in the final FIRAS CMB results (Mather et al. 1999). We report here the expressions used for the redshift z_{eq} and wavenumber of the particle horizon k_{eq} at the matter-radiation equality, in which $\Theta_{2.7} = \frac{T_{\mathrm{CMB}}}{2.7}$, as well as the expression used for z_{drag}

$$z_{\mathrm{eq}} = 2.5 \times 10^4\, \Omega_{\mathrm{m}} \Theta_{2.7}^{-4} - 1\,; \tag{A.1}$$

$$k_{\mathrm{eq}} = 0.0746\, \Omega_{\mathrm{m}} \Theta_{2.7}^{-2}\,; \tag{A.2}$$

$$z_{\mathrm{drag,\,b1}} = 0.313\, \Omega_{\mathrm{m}}^{-0.419} \left(1 + 0.607\, \Omega_{\mathrm{m}}^{0.674}\right)\,; \tag{A.3}$$

$$z_{\mathrm{drag,\,b2}} = 0.238\, \Omega_{\mathrm{m}}^{0.223}\,; \tag{A.4}$$

$$z_{\mathrm{drag}} = 1345\, \frac{\Omega_{\mathrm{m}}^{0.251}}{1 + 0.659\, \Omega_{\mathrm{m}}^{0.828}} \left(1 + z_{\mathrm{drag,\,b1}} \Omega_{\mathrm{b}}^{z_{\mathrm{drag,\,b2}}}\right)\,. \tag{A.5}$$

$$\tag{A.6}$$

Then we compute the distance r_{drag} as

$$R_{\mathrm{drag}} \equiv \frac{3\rho_{\mathrm{b}}(z_{\mathrm{drag}})}{4\rho_{\gamma}(z_{\mathrm{drag}})} = 31.5\, \Omega_{\mathrm{b}} \Theta_{\mathrm{CMB}}^{-4} \frac{1000}{1 + z_{\mathrm{drag}}}\,; \tag{A.7}$$

$$R_{\mathrm{eq}} \equiv \frac{3\rho_{\mathrm{b}}(z_{\mathrm{eq}})}{4\rho_{\gamma}(z_{\mathrm{eq}})} = 31.5\, \Omega_{\mathrm{b}} \Theta_{\mathrm{CMB}}^{-4} \frac{1000}{1 + z_{\mathrm{eq}}}\,; \tag{A.8}$$

$$r_{\mathrm{drag}} = \frac{2}{3k_{\mathrm{eq}}} \sqrt{\frac{6}{R_{\mathrm{eq}}}} \ln\left(\frac{\sqrt{1 + R_{\mathrm{drag}}} + \sqrt{R_{\mathrm{drag}} + R_{\mathrm{eq}}}}{1 + \sqrt{R_{\mathrm{eq}}}}\right). \tag{A.9}$$

The prefactor 1345 in Eq. (A.6) was taken from Eq. (E-2) in Hu & Sugiyama (1996) rather than the 1291 prefactor used in Eisenstein & Hu (1998) because we find a significantly better agreement with the results from the Boltzmann codes `CAMB` and `CLASS` (Blas et al. 2011). Varying h, Ω_{b}, or Ω_{m} in [0.6,0.8], [0.039,0.059], and [0.17,0.37] respectively while fixing the other parameters to the fiducial values of Flagship, we find an average relative difference $\frac{r_{\mathrm{s,\,drag,\,HS}}}{r_{\mathrm{s,\,drag,\,CAMB}}} - 1$ of -0.04%, 0.01%, and 0.03% using 1345 as a prefactor against $\frac{r_{\mathrm{s,\,drag,\,EH}}}{r_{\mathrm{s,\,drag,\,CAMB}}} - 1$ of 2.7%, 2.7%, and 2.6% using 1291.